CHAPTER IV

LIQUID MIRROR INFRASTRUCTURE

Generation of an operational LMT requires the integration of a variety of components each of which must satisfy stringent design requirements. The major components can be divided into two groups – the mirror subsystem and the prime focus assembly. The mirror subsystem consists of the mirror container and Hg, the air bearing and drive motor and air supply system, the supporting 3-point base, and the safety stabilizer. The prime focus assembly consists of the corrective optics, detectors, filters, motion stages and controllers, and the supporting superstructure. The properties and governing criteria for each group are discussed herein.

A. Angular Moment Stiffness and Load Capacity

Assuming the mirror subsystem is structurally sound in the sense that it is capable of supporting the axial load of the mirror and Hg, the single most important factor determining the viability of a liquid mirror is angular moment stiffness. The formation of the thin liquid Hg mirror surface requires that the mirror container and its supporting structure together satisfy an angular stiffness criterion against angular deflection (tilt). If the system does not possess adequate angular moment stiffness, then it will be unstable and a continuous Hg layer covering the mirror cannot be formed, or in an extreme event, catastrophic tipping of the mirror or damage to the air bearing could occur.

The mirror system must be stable with respect to the small angular tilt arising from moderate asymmetries in the distribution of Hg about the rotational axis. These occur primarily during the initial start-up and stabilization phase of LMT operation when the Hg has not yet attained equilibrium, but due to non-uniformity in the spun-cast surface, small scale asymmetries can exist at any time. If the mirror system is not adequately stiff, then these asymmetries can grow and the mirror can become unbalanced. If the imbalance then grows to exceed the angular load capacity of the air bearing, it will fail and internal damage will result.

As an example, when the mirror is started from its rest state, the central flat pool of Hg begins to spread over the mirror substrate. It does so unevenly and often develops significant asymmetries in the mass distribution of Hg. An azimuthal imbalance exceeding 20% of the total mass of Hg with an average radial position of 75 cm is not uncommon. For the NASA- LMT with 193 kg of Hg (1.61 mm film over 71,176 cm^2 with a 2.8 liter inner and outer channel) this corresponds to a 284 Newton-meter (N-m) torque. As a precaution the air bearing should have an angular load capacity which leaves a margin for safety. The PICo air bearing used with the NASA-LMT satisfies this criteria with a measured angular load capacity at NODO of approximately 700 N-m. To protect against loads which exceed even this value, the mirror perimeter is bounded by an emergency stabilizer with six rollers positioned with a small amount of clearance relative to the mirror perimeter. For angular loads exceeding 700 N-m, the mirror subsystem flexure allows the mirror perimeter to contact the stabilizer rollers and relieve the load,

thus protecting the air bearing. The roller-mirror clearance of 1.25 mm follows directly from the angular load limit and the subsystem angular moment stiffness discussed below.

The critical angular moment stiffness criteria can be determined by ensuring that the elastic energy of the system always exceeds the gravitational potential energy under tilt perturbations. This ensures that the restoring force is always sufficient to prevent instability. Content (1992) and Hickson et al. (1993) have shown that for a system where the mirror container deformation is neglected (ie. the volume of tilt displaced Hg is for a rigid mirror only) the system will be stable if the angular moment stiffness exceeds the critical stiffness (k_{crit}) given by:

$$k_{crit} = \left[\sum_i \left(\frac{1}{k_i} \right) \right]^{-1} = \frac{\pi \rho g R^4}{4} \qquad \text{(IV.A.a)}$$

Where:

$k_i =$ the angular stiffness of an individual system component (eg. air bearing, mirror, etc.)

$\rho = \rho_{Hg} =$ density of Hg ($13.546\, g/cm^3$ at $20\ ^0C$)

g = gravitational acceleration ($981.67\ cm/\sec^2$ at NODO)

R = Mirror radius (150 cm for NASA-LMT)

For the NASA-LMT this equation implies that the inverse sum of the reciprocal

angular moment stiffness values for the individual mirror system components must exceed $5.287x10^{12}\ dyne \cdot cm$/rad (or $5.287x10^{5}\ N \cdot m$/rad) in order for the mirror system to be stable.

For the NASA-LMT, the integrated components of the mirror system have a combined angular moment stiffness of $8.271x10^{5}\ N \cdot m$/rad which exceeds the critical value by a factor 1.56 and thus the NASA-LMT is stable with respect to tilt perturbations. Figures IV.A-1 and 2 show the measured angular moment stiffness values for the air bearing separately and the integrated mirror sub-system. These measurements were conducted by placing known loads at various points within the system and measuring the resulting deflections. Differencing the air bearing and its interface compliance of $3.81x10^{6}\ N \cdot m$/rad, the mirror container compliance of $1.78x10^{6}\ N \cdot m$/rad (as measured by Hickson in his laboratory after he constructed the mirror), and the total system compliance, yields an angular moment stiffness of $2.60x10^{6}\ N \cdot m$/rad for the I-Beam base portion of the system.

B. Air Bearing

An air bearing uses a thin film of pressurized air as the supporting medium between the rotor and stator. The air film is analogous to the hydraulic fluid of a hydrostatic bearing or the balls and rollers of a mechanical bearing. Utilizing an air bearing for the LMT obviates the viscous drag of the hydrostatic bearing or the

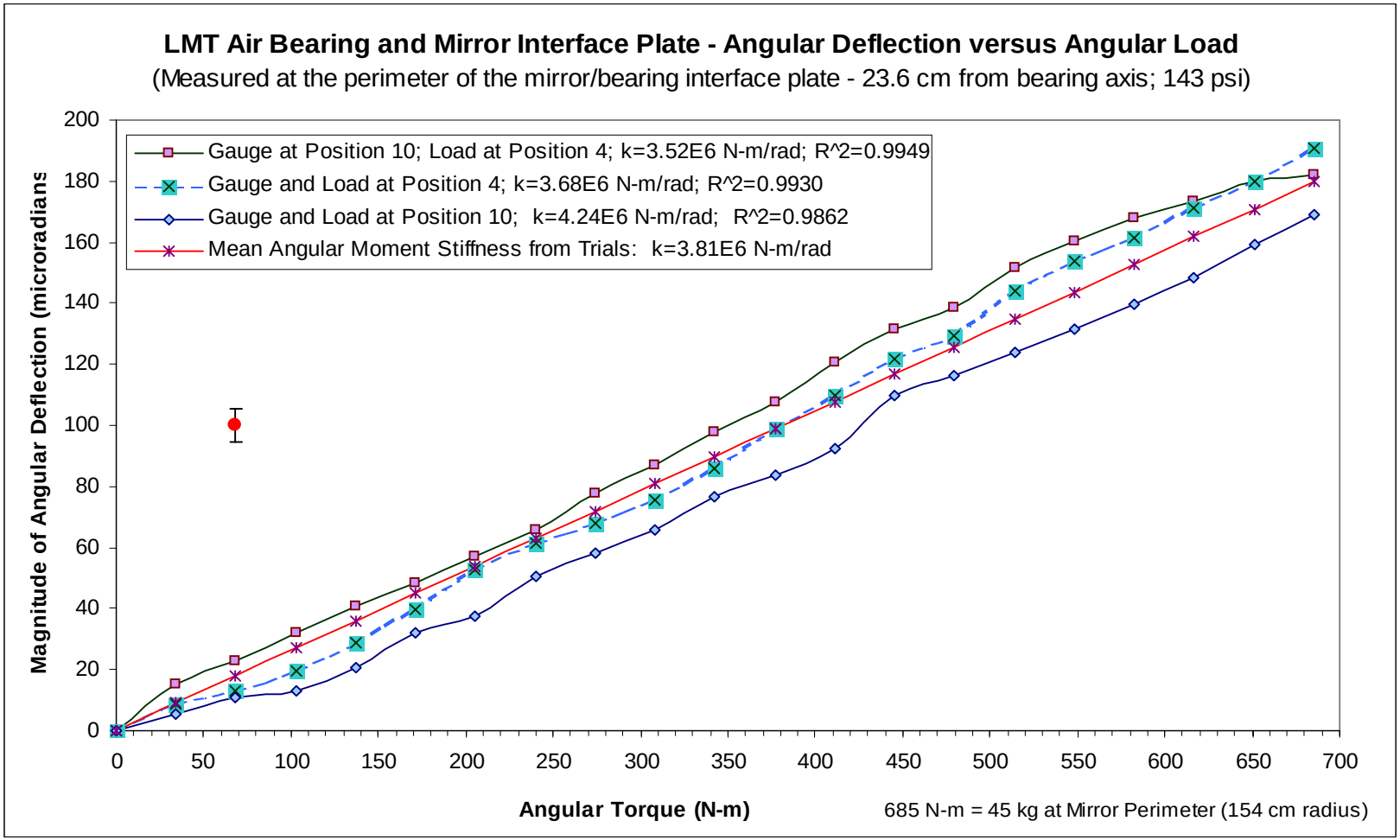

Figure IV.A-1. The angular moment stiffness of the air bearing coupled with the mirror interface plate and surface mounting. The mean stiffness differs from the air bearing specification (13.60E6 N-m/rad) because of flexure in the interface plate and mounting surfaces and slightly reduced operating pressure. The bearing is loaded with the mirror container (160 kg) and 14.24liters of Hg (193 kg). Error bar in red.

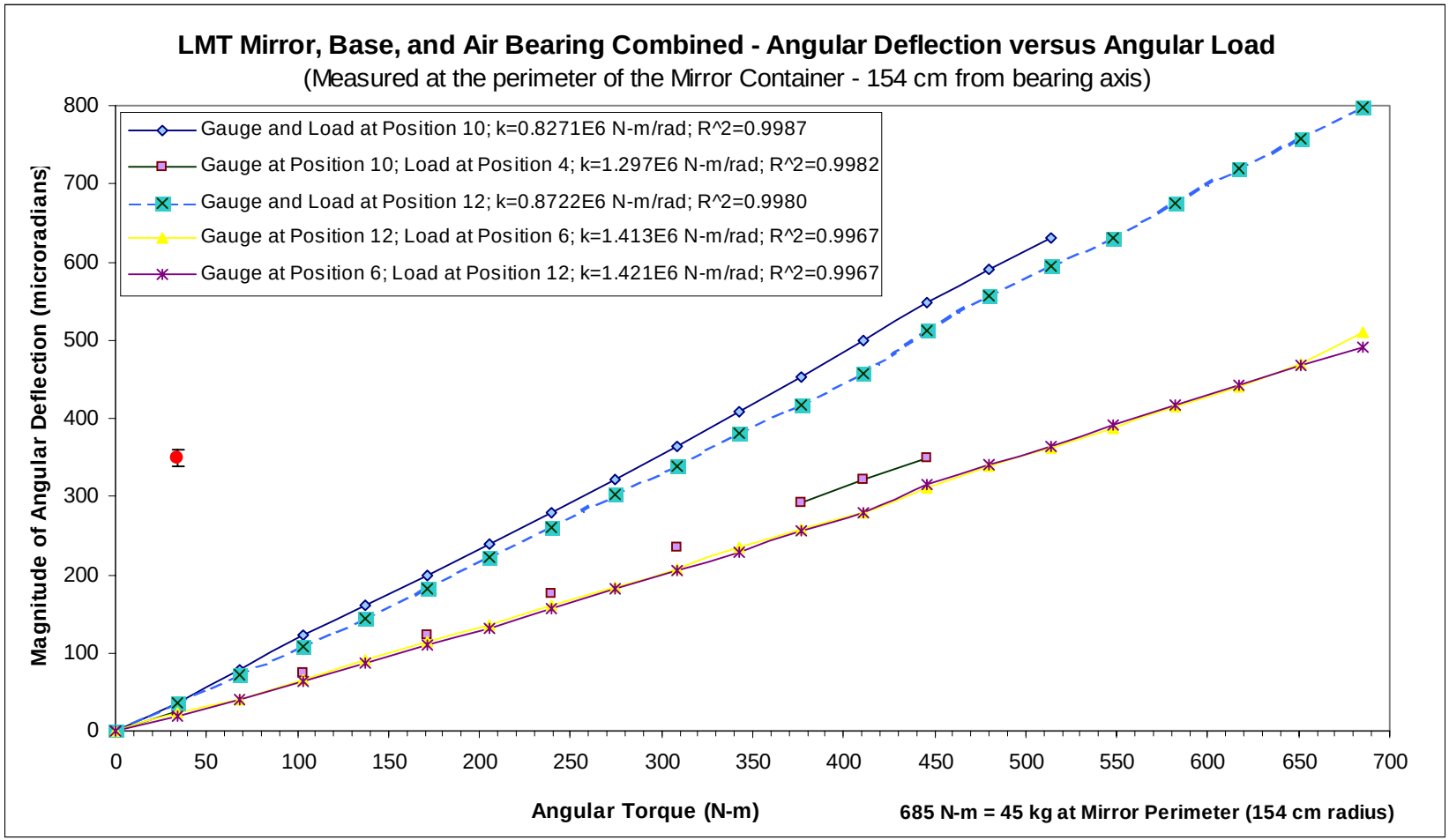

Figure IV.A-2. A graph demonstrating the angular moment stiffness of the fully loaded mirror sub-system. The difference between the grouped upper and lower traces is attributed to flexure in the mirror container. The minimum measured stiffness (upper curve; 8.271E5 N-m/rad) exceeds the minimum requirement for the NASA-LMT of 5.287E5 N-m/rad by a 1.56 safety factor. Internal bearing contact occurs for angular loads above 700 N-m. Error bar in red.

mechanical vibrations of the ball/roller bearing arising from the internal contact between rolling surfaces. Air bearings also have smaller error motion than these alternatives. As discussed throughout, the NASA-LMT uses the 10R Universal Air Bearing Spindle from Professional Instruments Company (PICo). A much larger bearing (20R) from the same manufacturer is being used on the 6m LZT.

The PICo bearing was chosen because its grove-compensated design is inherently immune from oscillatory instabilities like that exhibited in the Warren inlet-restricted orifice air bearing used unsuccessfully in the initial NASA-LMT development effort. Additionally, the PICo bearing possessed an axial and angular load capacity, angular stiffness, and error motion that exceeded the specifications of all other commercially available air bearings. As such it easily supports the 3367 N axial load of the mirror container and Hg, with its 12,850 N ultimate axial capacity (at full operating pressure). This excess capacity is important because the axial and angular load capacities are coupled in the sense that a load applied in one mode reduces the other capacity proportionally. Additionally, capacity and stiffness values vary linearly with air pressure up to the maximum operating pressure of 150 psi. Since the NASA-LMT operates at 143 psi the ultimate values are not fully realized. For the NASA installation, accounting for the reduced operating pressure and mode coupling, the PICo air bearing is 27.5 % axially loaded and the ultimate angular load capacity implied by the 700 N-m measured value is thus 1013 N-m. This ultimate angular load capacity exceeds the published specification of 544 N-m by 86%.

The PICo air bearing axial and radial error motion are each less than 25.4 nm and

the tilt (coning) error is only 0.021 arcseconds. This compares very favorably with values for traditional hydrostatic or mechanical bearings which at best have axial and radial total indicator motions of several microns and coning errors of ~1 arcsecond. Because of its simplicity, Tremblay and Borra (2000) assembled a liquid mirror with a mechanical bearing, but the resultant mirror quality was unacceptable due to the large (1.5 arcsecond) coning error.

C. Air Supply System

Unlike mechanical bearings or some hydrostatic bearings, the air bearing does require extensive infrastructure support in the form of an air supply system and emergency breaking system. The breaking system is necessary to ensure that the air bearing is always pressurized while rotating. If a power failure or some arbitrary event causes an air system failure, then the air bearing rotation must be stopped before it depressurizes. Electrical pressure sensors installed throughout the air supply system are linked to a spring-loaded solenoid attached to a brush below the mirror. If the system pressure drops below the nominal air bearing operating pressure, the solenoid de-energizes and the brush engages the mirror bringing it gently to a halt within 60 seconds. A secondary pressurized nitrogen supply operating at a pressure sufficient to fully support the air bearing will automatically engage via a shuttle valve if a catastrophic line rupture occurs in the primary system.

As shown in Figure IV.C-1, the NASA-LMT primary air system uses a 5 HP

NASA-LMT @ NODO: Air System Configuration

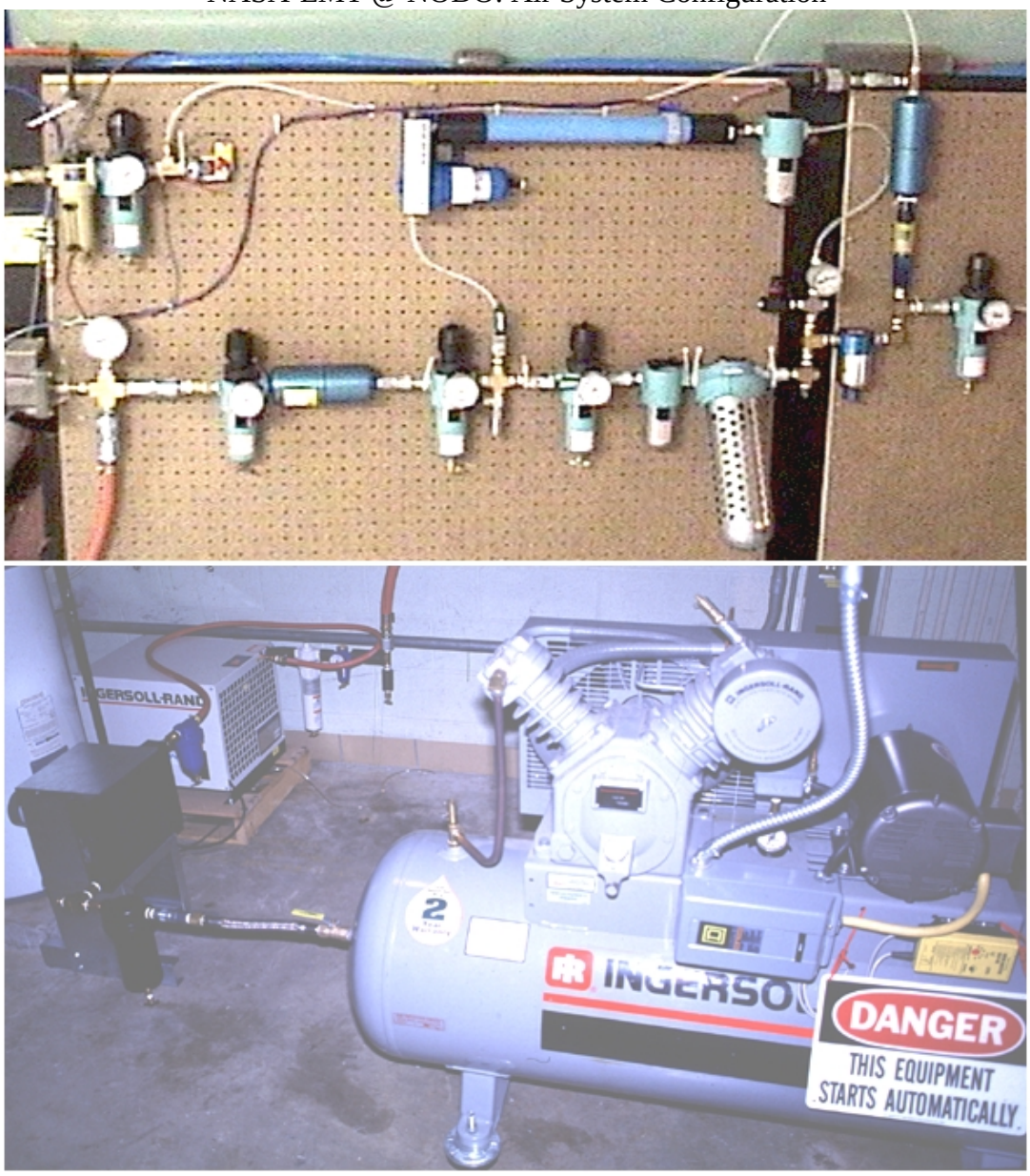

Figure IV.C-1. Views of the upper and lower stages of the NASA-LMT air system. The lower stage (bottom photo) consists of the two-stage 5 HP (horsepower) air compressor with its 80 gallon accumulator, an after-cooler, oil separators, refrigerated dryer, and first-stage regulators. The upper stage consists of a series of filters, regulators, pressure sensors, a primary membrane dryer, and backup desiccant dryers. The final output has a pressure of 143 psi (lbs/in^2), a –35 ^0C dew point and a flow capacity of approximately 5 SCFM (standard cubic feet/minute). The secondary nitrogen supply regulators are visible at the upper left. A portion of the final output is sent to the CCD camera for dew removal via the regulator at the far right of the upper photo. Apart from a weekly draining of the lower stage filters and an occasional bake-out of desiccant, the air system requires no maintenance.

(horsepower) two-stage compressor with an 80 gallon accumulator coupled to a series of oil separators, dryers, filters, and regulators to supply the air bearing continuously with air at a constant pressure of 143 psi (lbs/in^2), a –35 ^0C a dew point, and a 2 SCFM (standard cubic feet per minute) flow rate. The bearing's mild steel construction and tight internal tolerances (2.8 um clearance) also require that the inlet air be extremely clean and dry to prevent particulate contamination or moisture condensation within the bearing. The air supply is filtered to remove particles with diameters larger than 1 um and the –35 ^0C dew point ensures that the bearing is protected from condensation even under the coldest conditions recorded at NODO (-12 ^0C). A large margin of safety is provided for the Joule-Thompson expansion within the air bearing which effectively increases the air supply dew point by several degrees centigrade (Dahl PC). The air bearing is also shrouded with a clear LEXAN cover so that it is bathed in its own exhaust air to protect the exterior from corrosion.

Since the PICo air bearing's stiffness and load capacities depend linearly on air pressure, it is critical that the bearing operate at a constant pressure as close as possible to its maximum operating pressure of 150 psi. Variations in operating pressure translate into variations in angular moment stiffness which can then affect the dynamic balance of the mirror (Chapter V) with a consequent deleterious effect on image quality by introducing mirror wobble. A total of 5 pressure regulators in the primary air system ensure a stable operating pressure of 143 psi to within 0.5 psi (0.3 %).

Figure IV.C-2 shows the air bearing internal lift as a function of air pressure while

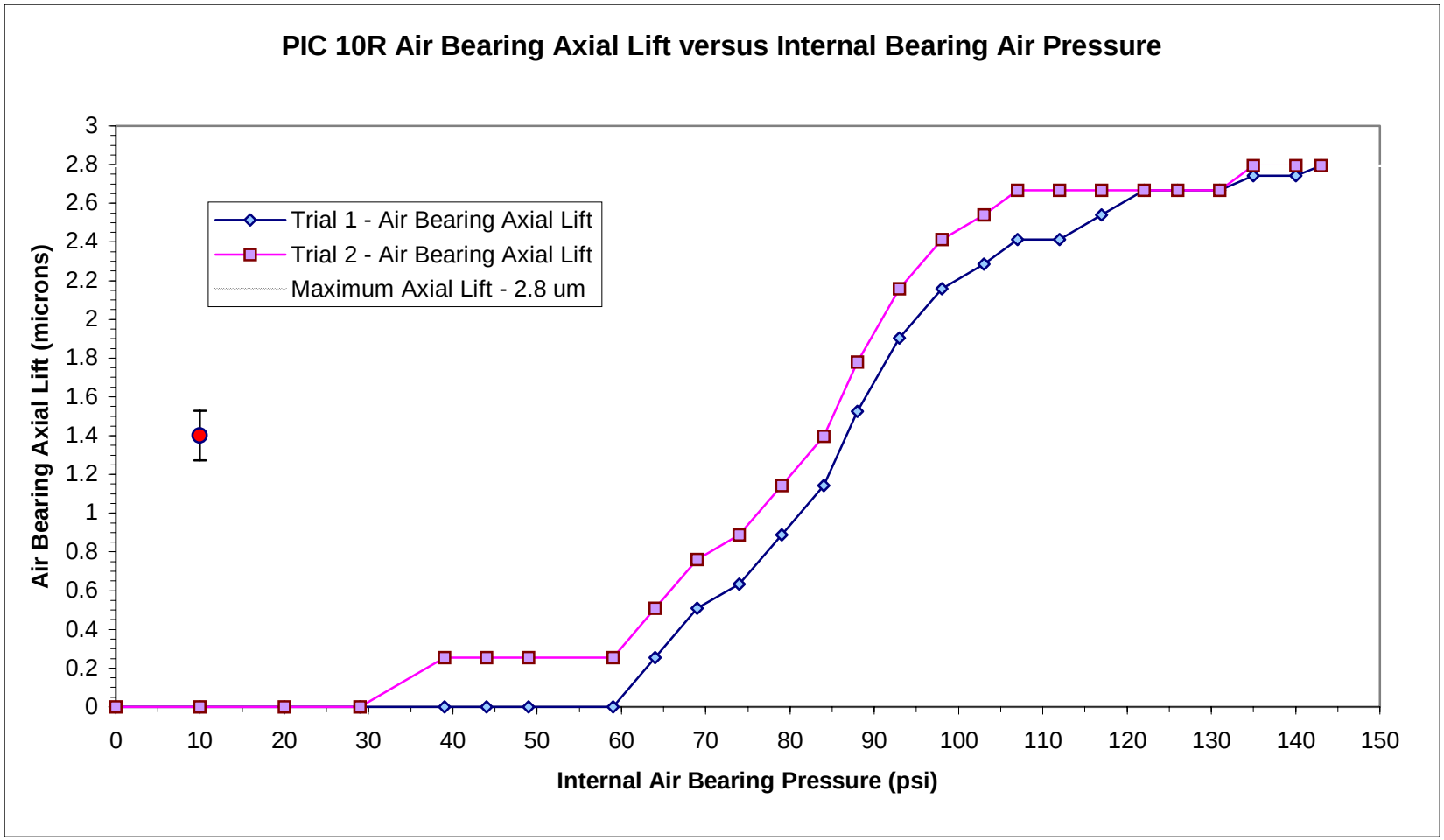

Figure IV.C-2. A graph demonstrating vertical lift of the air bearing load plate as a function of applied journal air pressure. The bearing is fully loaded with the mirror container (160 kg) and 14.24liters of Hg (193 kg). Accounting for both sets of measurement trials, the bearing is fully floating at 135 psi. Normal operating pressure is 143 psi. Measurement error bar is indicated in red.

fully loaded with the NASA liquid mirror. The air bearing rotor floats at pressures above 60 psi and attains it maximum lift of 2.8 um at approximately 135 psi which sets a nominal lower pressure limit for operations. Even when the mirror is dormant, a bearing pressure of 65 psi is maintained to prevent capillary action from drawing moisture into the bearing structure.

D. I-Beam Base and Pier

The base upon which the air bearing and mirror rest must serve two critical functions. It must rigidly couple the system to the pier and it must enable precision leveling of the entire assembly (axial parallelism with g). Initially, it was decided to use as the base three I-Beam segments welded in the form of a triangle. Although this design yielded a large footprint to facilitate leveling with screws at each vertex, it is not as rigid as would be a compact monolithic structure. Such an alternative has been designed, but not yet implemented. In the interim, it has been necessary to stiffen the I-Beam structure by adding additional welds as well as supporting pads between the midpoints of the triangle and the pier. For added rigidity each 1-40 leveling screw mates to the pier top plate via 1-inch diameter spherical gauge balls and lapped brass pads. These provide strong coupling between the base and pier and enable 0.1 arcsecond leveling accuracy. Figure IV.D-1 shows the base and air bearing beneath the NASA 3m liquid mirror as installed at NODO. Figure IV.D-2 shows a close-up of one of the brass pads.

The interface between the I-Beam base and the air bearing assembly consists of a

NASA-LMT @ NODO: Primary Mirror Undercarriage

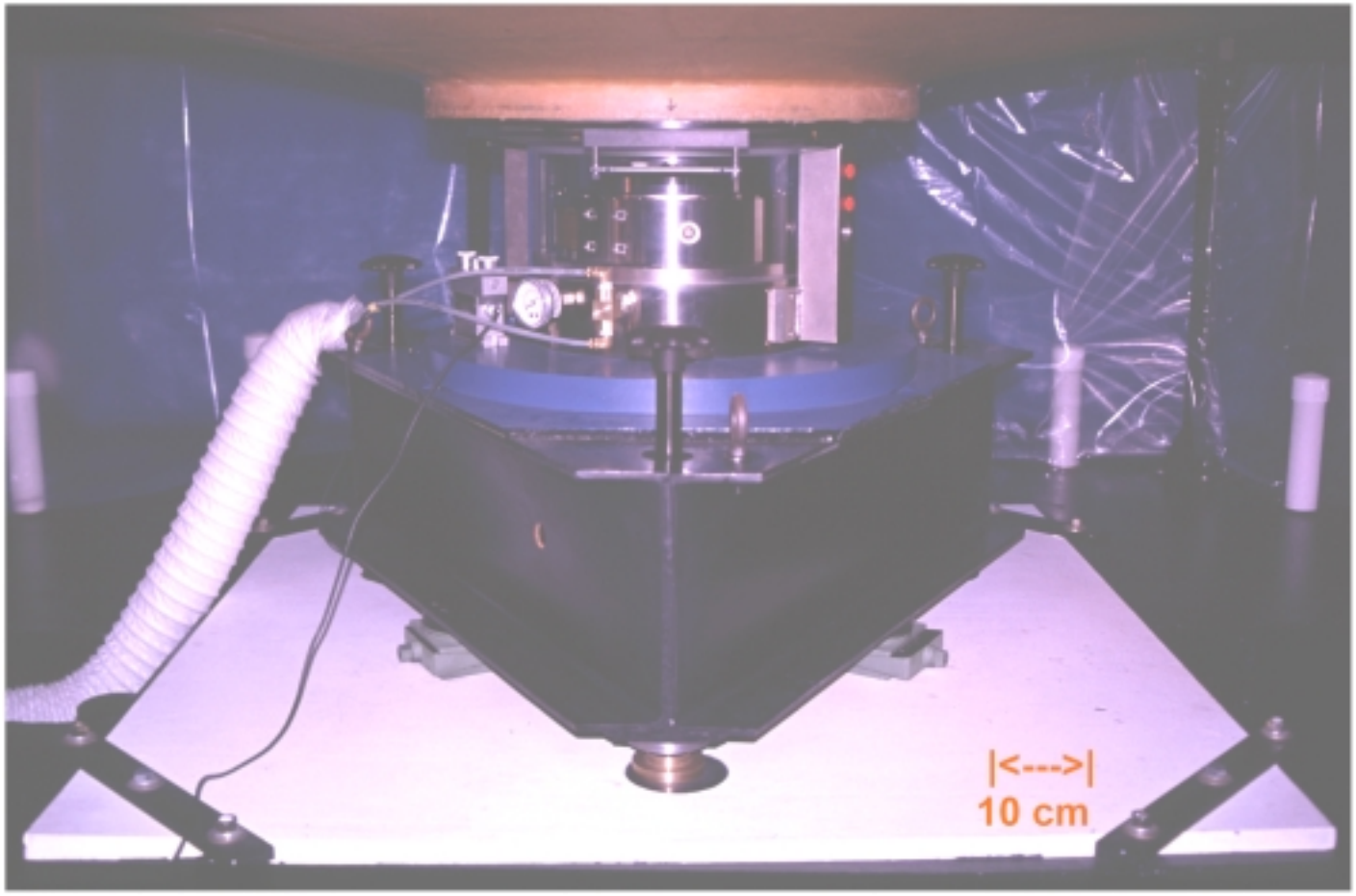

Figure IV.D-1. View of the undercarriage of the NASA-LMT showing the PICo air bearing and the I-beam base with the modified 3-point suspension system. The three leveling screws which protrude through the base have handles affixed (black stems). The white pier plate is grouted and strapped to the pier top. Three coarse pads (green) are located at the midpoint of each base leg to add additional stiffness.

NASA-LMT @ NODO: I-Beam Base - Leveling Screw, Gauge Ball and Pad

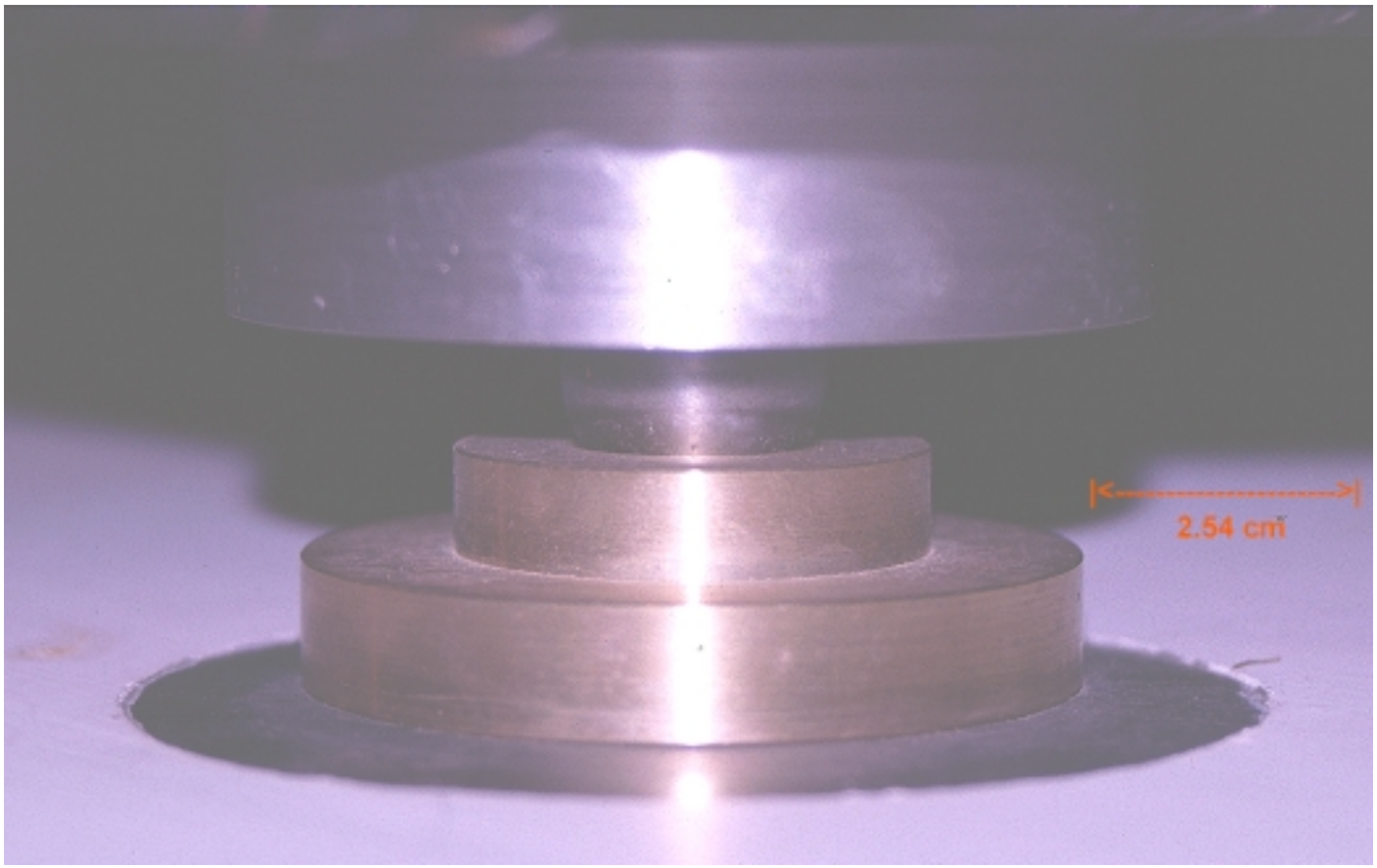

Figure IV.D-2. View of one of the three assemblies employed to level the NASA 3m primary mirror. The assemblies are located at each of the vertices of the triangular I-Beam base. They consist of a 1-40 machined screw (with only 12.7 um (0.0005 inch) thread clearance) coupled to a 2.54 cm (1-inch) diameter gauge ball which is then lapped to a brass pad which itself is lapped to the pier top plate. The interface contributes to the relatively high $2.60x10^6\,N\cdot m$/rad angular moment stiffness of the I-Beam base, and allows leveling to 0.1 arcsecond.

3.81 cm (1.5-inch) thick circular steel plate bolted directly to the top of the I-Beam base and bedded with epoxy to reduce flexure. The top surface of this plate is ground flat to 12.7 um (0.0005-inch). The air bearing itself resides within a Stainless Steel carriage which bolts directly to the I-Beam plate via a 12-bolt circle to provide uniform loading. The carriage was necessary to provide lifting points, a fixture for the cylindrical LEXAN anti-corrosion cover, and a mounting surface for the direct drive motor. The motor stator is bolted to the air bearing carriage while the motor rotor connects to the air bearing rotor. The motor assembly drops through a central hole in the I-Beam plate and motor access is obtained by reaching between the bottom of the I-Beam base and the pier.

E. Mirror-Bearing Interface and Stabilizer

In order to protect the air bearing from the application of an angular load exceeding its design capacity, the mirror is not bolted to the air bearing but rather has a relieved (4 mm deep) circular aperture (50 cm diameter) which slides over the air bearing interface plate. The mirror is thus precisely centered, but is allowed to tip if sufficient torque is applied in a vertical plane. An approximately 470 N force (47 kg load; 690 N-m torque) applied at the mirror perimeter will tilt it such that it rests on both the vertical stabilizer at its outer perimeter, and the edge of air bearing interface plate at its lower hub. In such a state the stabilizer bears the tilting load, but the air bearing bears essentially the full 3367 N weight of the mirror at a point near the edge of the 50 cm diameter interface

plate. This places an angular load of 842 N-m on the air bearing which is 1.20 times the operational angular load capacity of 700 N-m. Although the approach is sound, the interface plate is too large to protect the air bearing. If its size were reduced to 41 cm diameter, then the angular load would be reduced proportionally to 690 N-m, within the operating angular load capacity limit. To compensate for this lack of protection, the six stabilizer rollers are set with a clearance such that the mirror subsystem flexure will enable contact with the stabilizer if the angular load exceeds the 700 N-m operational limit. The mirror stabilizer is shown in the upper portion of Figure IV.E-1 prior to attachment of the individual rollers. The lower image shows an installed roller prior to setting the 1.25 mm clearance between the mirror edge and rolling surface. Under routine operations, the mirror never touches the stabilizer rollers, they are only meant as a contingency device to prevent damage to the bearing or a catastrophic spillage of mercury if the mirror were accidentally impacted by a heavy object. This was not the case with the Warren air bearing which, because of poor angular stiffness ($0.967.x10^{6}\ N \cdot m$/rad), required the stabilizer during the initial start-up of the mirror wherein the normal asymmetries in the Hg distribution were sufficient to damage the bearing.

F. Mirror Container and Spun-cast Surface

The composite mirror container used for the NASA-LMT was designed by Hickson et al (1993). It is an extremely lightweight yet rigid structure which is able to resist distortion from both the axially symmetric and asymmetric Hg loads that occur

NASA-LMT @ NODO: Mirror Stabilizer and Roller

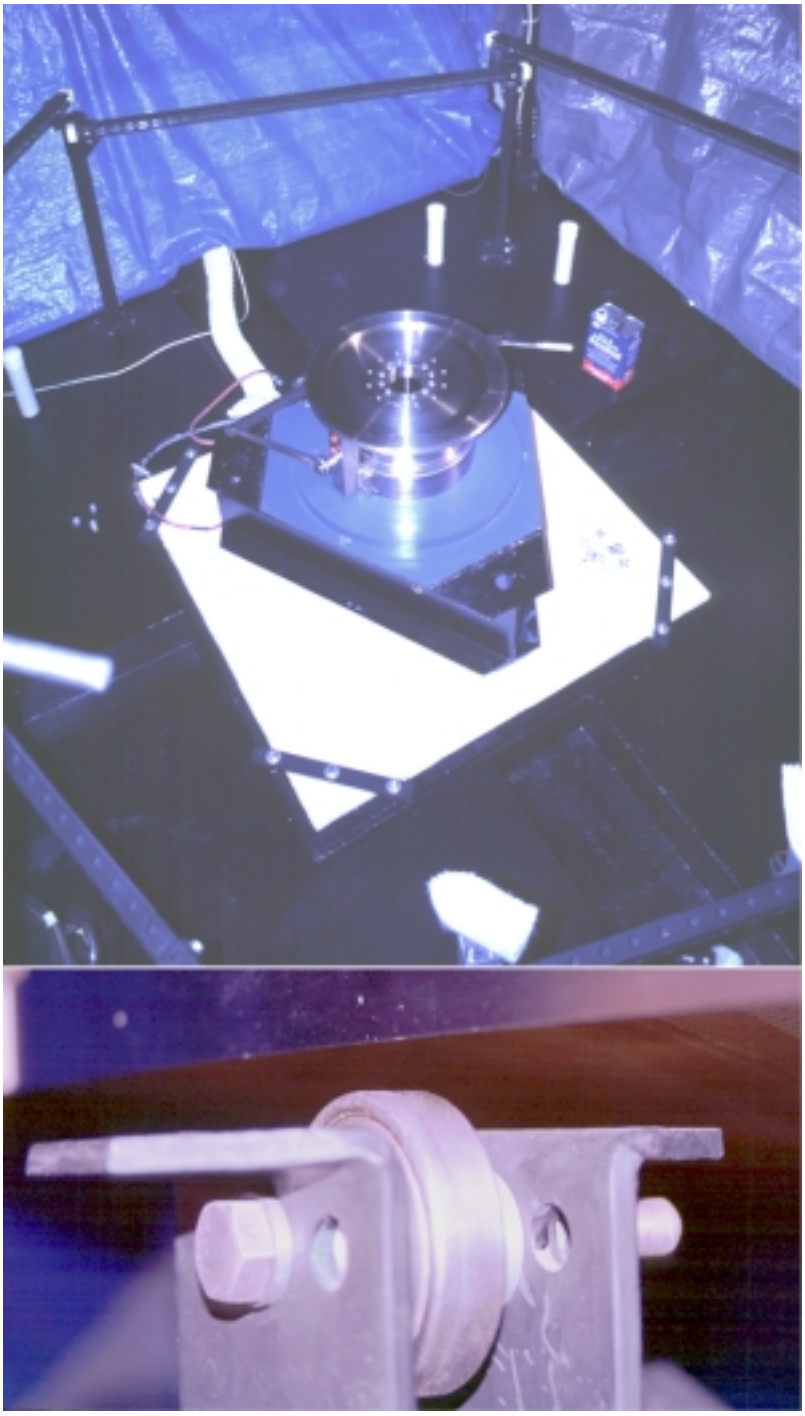

Figure IV.E-1. The upper image is a view of the mirror stabilizer prior to installation of the NASA 3m liquid mirror at NODO. The lower image shows an individual roller prior to setting the 1.25 mm clearance between it and the mirror edge.

during LMT operations. As described briefly in Chapter I, the upper substrate is spun-cast polyurethane and as such its quality is subject to a variety of factors including cleanliness of the environment, ambient temperature, mixing technique and mixing ratios, and the potential entrapment of air in the uncured liquid polyurethane. Without rigid quality control and extensive practice, it is difficult to generate a spun-cast surface with maximum deviations of less than 0.1 mm from that of a parabola. For the NASA- LMT spin-casting was performed twice and the deviations are still of order 0.3 mm. Deviations larger than this have been individually removed by hand sanding. Surface imperfections must be minimized because they make it difficult to establish a thin Hg surface. At the NASA-LMT it has not been possible to maintain continuously an Hg layer thinner than 1.61 mm. Below this thickness it is extremely difficult to establish the Hg surface because it separates at the surface imperfections. Figure IV.F-1 illustrates the measurement of vertical run-out and surface deviations with a dial indicator mounted near the mirror perimeter.

In addition to the localized imperfections, the NASA-LMT appears to exhibit a small vertical sag at the mirror perimeter and a periodic radial deformation in the surface. The sag, possibly related to the mirror's long-term response to the Hg load or to the lower NODO operating temperature relative to NASA-JSC, yields a slightly thicker Hg layer (by a few percent) at the mirror edge relative to the mirror center. The periodic radial deformation is more serious. It appears in the form of six annular recesses, each one occurring at the boundary between the individual equal-area annuli into which the

NASA-LMT @ NODO: Measurement of Mirror Surface Deviations

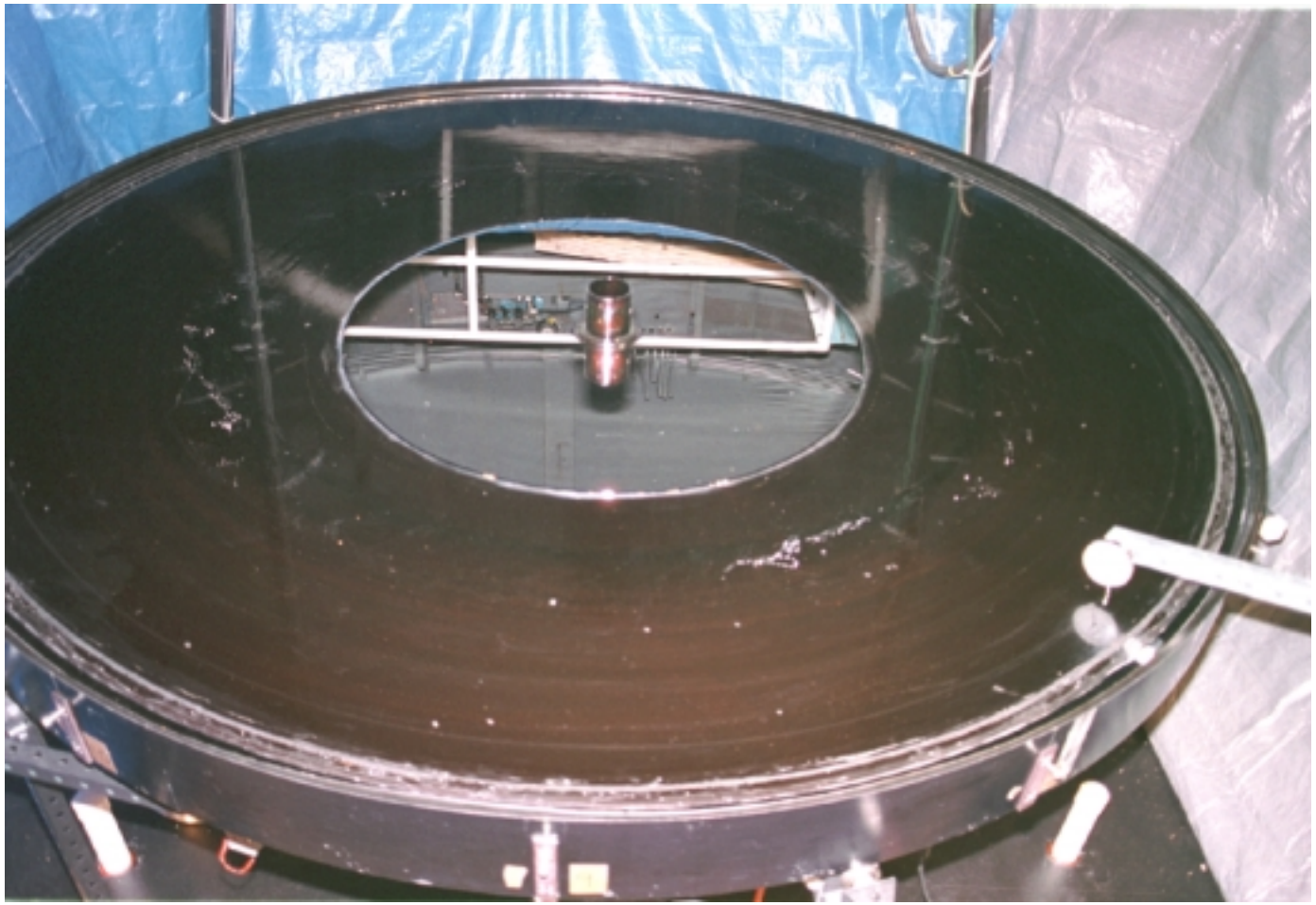

Figure IV.F-1. Measurement of mirror vertical run-out and surface deviations with a dial indicator. The spun-cast polyurethane surface is parabolic, but has localized defects protruding as much as 0.3 mm above the mirror surface.

liquid polyurethane was poured. The deformation is evident as print-through to the Hg upper surface in the out-of-focus entrance pupil images as discussed in Chapter V.

As mentioned in Chapter I, Hickson has devised an alternative to the composite spun-cast mirror container. His design for the 6 m LZT utilizes a mirror substrate comprised of machined hexagonal segments bonded together as a membrane and supported at 19 adjustable points by a lightweight steel space frame. The adjustable nature of the membrane will enable a parabolic surface accurate to 0.1mm to be mechanically generated, obviating the uncertainty associated with spin-casting. The LZT is expected to be operational in 2001.

G. Direct-drive Motor and Controller

Maintaining constant angular velocity of the rotating mirror while minimizing the introduction of impulse or vibration requires a smooth drive motor with minimal cogging and torque ripple. Brush-less (Byers PC) or Eddy current (Dahl PC) motors satisfy these requirements, but tend to have intrinsically low torque. Fortunately, because the liquid mirror is manually brought from rest to its operating angular velocity, a low torque motor is sufficient since it must only compensate for the drag associated with air moving past the rotating mirror container and Hg surface. (The air bearing internal drag is comparatively negligible). Because the cost of an Eddy current motor was prohibitive, the NASA-LMT utilizes a 12-pole three phase brush-less DC motor with 2.14 N-m (Newton-meter) torque from MFM Incorporated (Model 089-0.75) with a sinusoidal linear

amplifier from Motion Control Systems (MCS LA2000 1996). The motor is directly coupled to the air bearing as shown in Figures IV.G-1 and 2, thus eliminating the complication of a belt-drive system used in previous LMTs (Hickson et al 1993, Borra et al. 1985a). Because of its low torque, the motor dissipates only 22 watts and thus presents a minimal heat source beneath the mirror. Convective heating from the motor has not been detected in either the radius of curvature or off-axis pupil images.

As shown together in Figure IV.G-3, the MCS LA2000 linear amplifier utilizes a Stanford Research Function Generator with a sine output and a 0.01 ppm time base as its frequency reference. The stability of the motor driving frequency is thus two to three orders of magnitude greater than the actual rotational stability of the mirror (Chapter III, Section D) as measured by a 1024 count optical encoder on the motor shaft. The use of feedback has not yet been employed to ascertain whether or not it is possible to correct the 1 to 30 ppm angular velocity variations experienced by the mirror due to convection and air movement. It is suspected that the use of feedback in a closed-loop configuration will not eliminate the angular velocity variations because they occur on short time-scales (~1 to 6 seconds) and the system inertia is too large to respond quickly to the application of a compensating torque. A feedback option is available with the MCS LA2000 linear amplifier and a preliminary evaluation of closed-loop operation is planned.

Since the motor is brush-less, there is no physical contact between the rotating and stationary portions of the portions of the mirror sub-system. This enables static charge to accumulate as the mirror spins in the air or as Hg moves over the polyurethane substrate (friction induced tribo electricity). This charge must be dissipated or it will discharge

NASA-LMT: PICo 10R Air Bearing with Mirror Interface and Motor Rotor

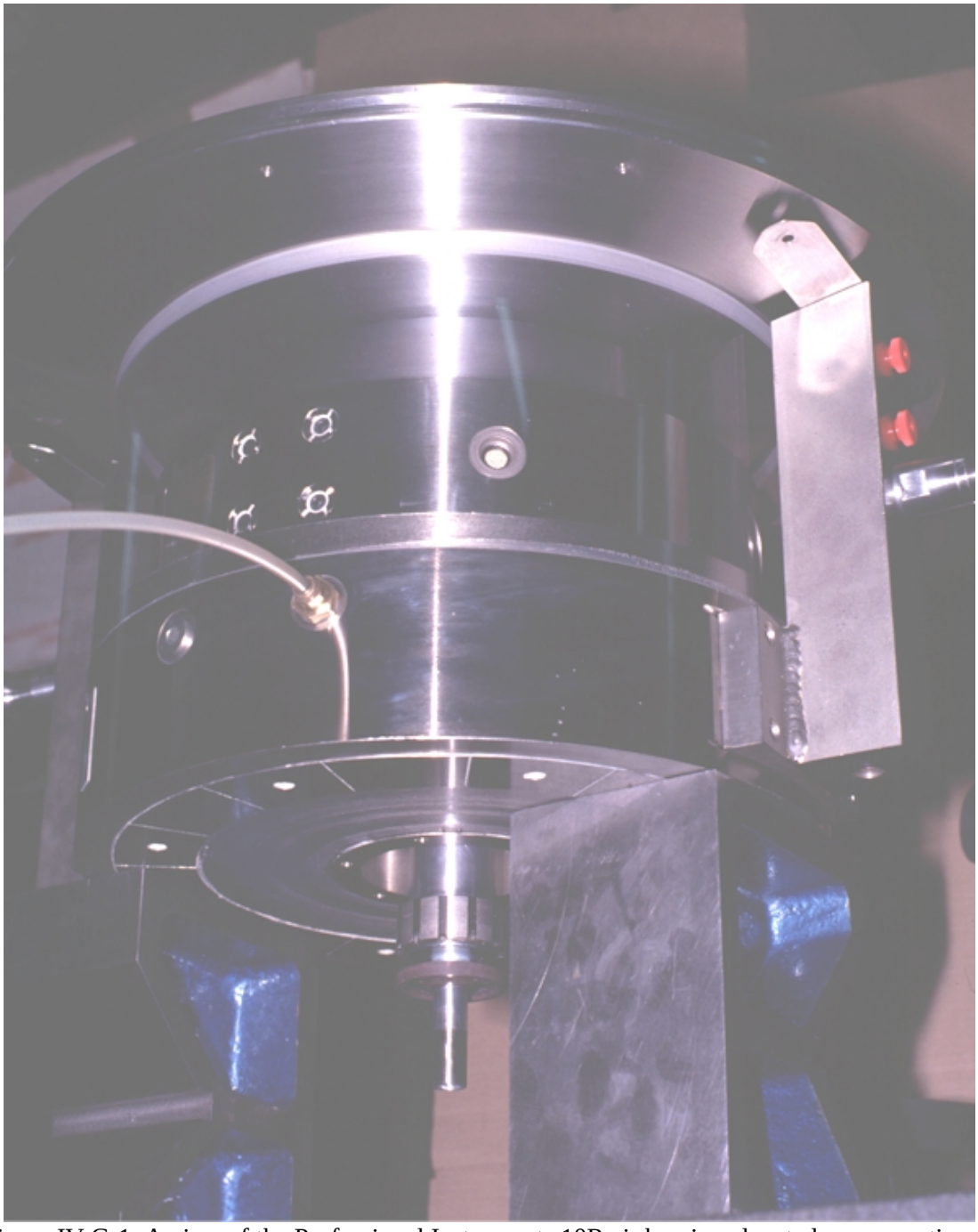

Figure IV.G-1. A view of the Professional Instruments 10R air bearing elevated on supporting blocks at the vendor's Minnesota headquarters. The actual air bearing is interior to the LEXAN sleeve which is part of a carriage built to enable the bearing to interface easily with the I-Beam base and the MFM 12-pole brush-less DC motor. The motor rotor with its twelve permanent magnets is visible extending downward from the bearing through the bottom of the carriage. The mirror interface plate is visible at the top. A pressurized air line is seen entering at the side.

NASA-LMT: Motor Installation on the PICo 10R Air Bearing

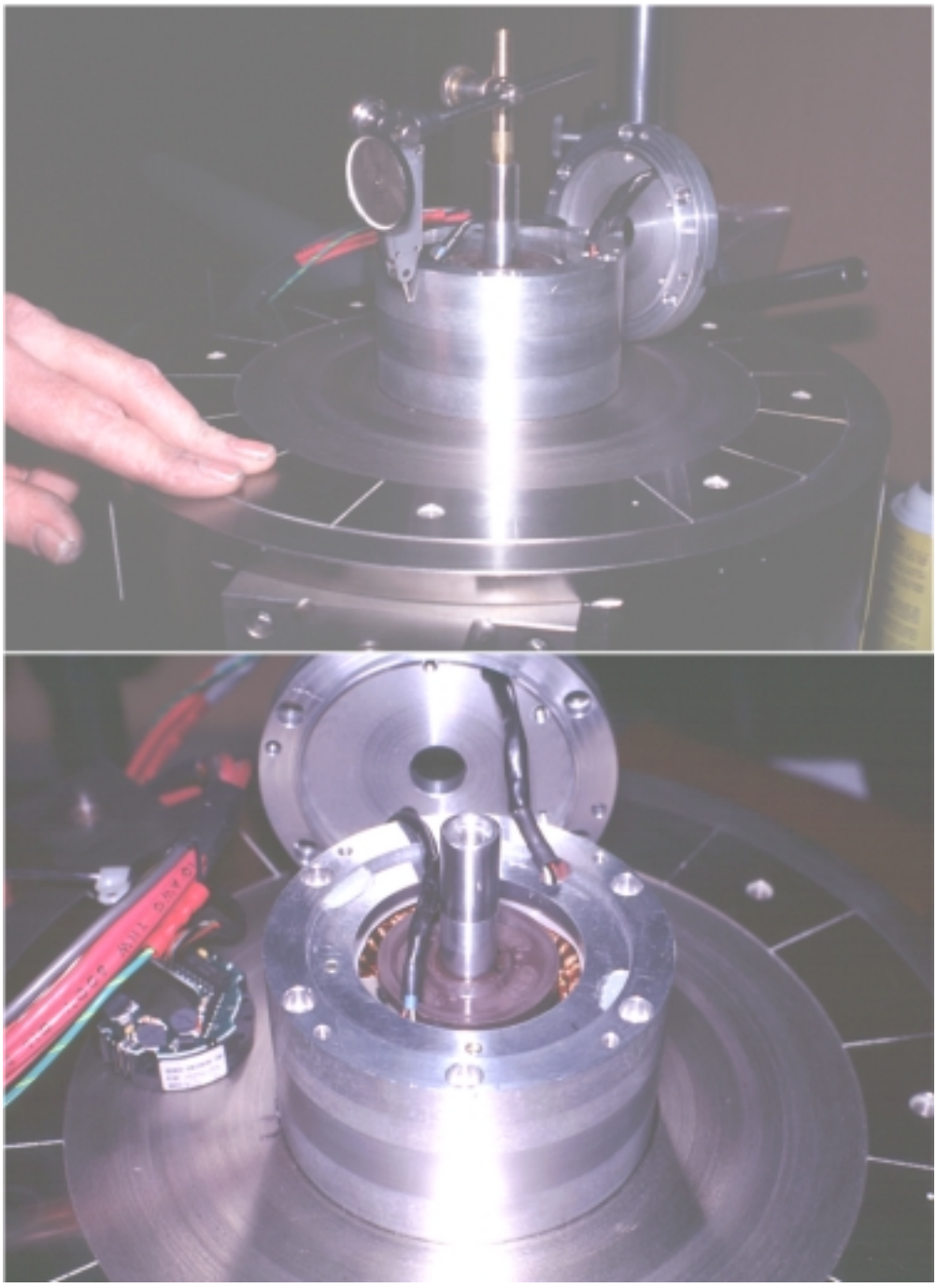

Figure IV.G-2. Installation of the MFM brush-less DC motor on the PICo air bearing carriage. In these inverted views, the motor is seen mounted on the base of the air bearing carriage. In the upper image, the stator is being aligned with respect to the rotor shaft with a dial indicator. In the lower image, a magnetized wheel and Hall-effect sensor package for rotation and commutation determination is visible on the rotor shaft. The 1024 line count optical encoder has been removed and rests at left.

Figure IV.G-3. A view of Motion Control Systems (MCS) LA2000 3-phase sinusoidal linear amplifier with the Stanford Research Systems (SRS) function generator and 0.01 ppm time base. In the normal open-loop configuration, the function generator provides a fixed reference signal from which the linear amplifier generates a 3-phase sinusoidal output to drive the MFM 12-pole brushless DC motor that is directly coupled to the PICo air bearing .

within the 2.8 um gap between the air bearing rotor and its stator, resulting in pitting and scoring of the interior bearing surfaces. To bleed the static charge a rotating mercury contactor (introducing negligible drag) from Mercotac Incorporated (Dahl, PICo PC) is mounted on the motor rotor shaft and wired to the grounded stator chassis.

H. Mercury (Hg)

Mercury (Hg) has been selected for use in LMTs because other materials have properties which make them unsuitable from an optical perspective. Mercury is highly reflective at optical and infrared wavelengths as shown in Figure IV.H-1, is in a liquid state above $-38.842\,^{0}C$, and is relatively inexpensive at approximately $15/kg. The only disadvantage to the use of mercury in LMTs is its toxicity, but this is a tractable problem - especially in the colder high-altitude environments where observatories are normally located. A demonstration of the relatively benign nature of Hg in cooler environs relative to warmer locales is explored in detail later in this section.

To otherwise circumvent the toxicity issue through the use of other materials, experiments (Borra 1994, Byers and Gibbons PC) have been performed on the suitability of both Gallium (Ga), which has a melting point of $29.78\,^{0}C$,and its eutectics which have melting points as low as $5\,^{0}C$ (Gallium:Indium:Tin). Gallium does not appear to be toxic (Sheka et al. 1966) so its exorbitant expense of approximately $4000/kg may seem justifiable. Unfortunately, however, an opaque skin forms over its otherwise highly reflective surface when it oxidizes making it unsuitable for use in LMTs unless the

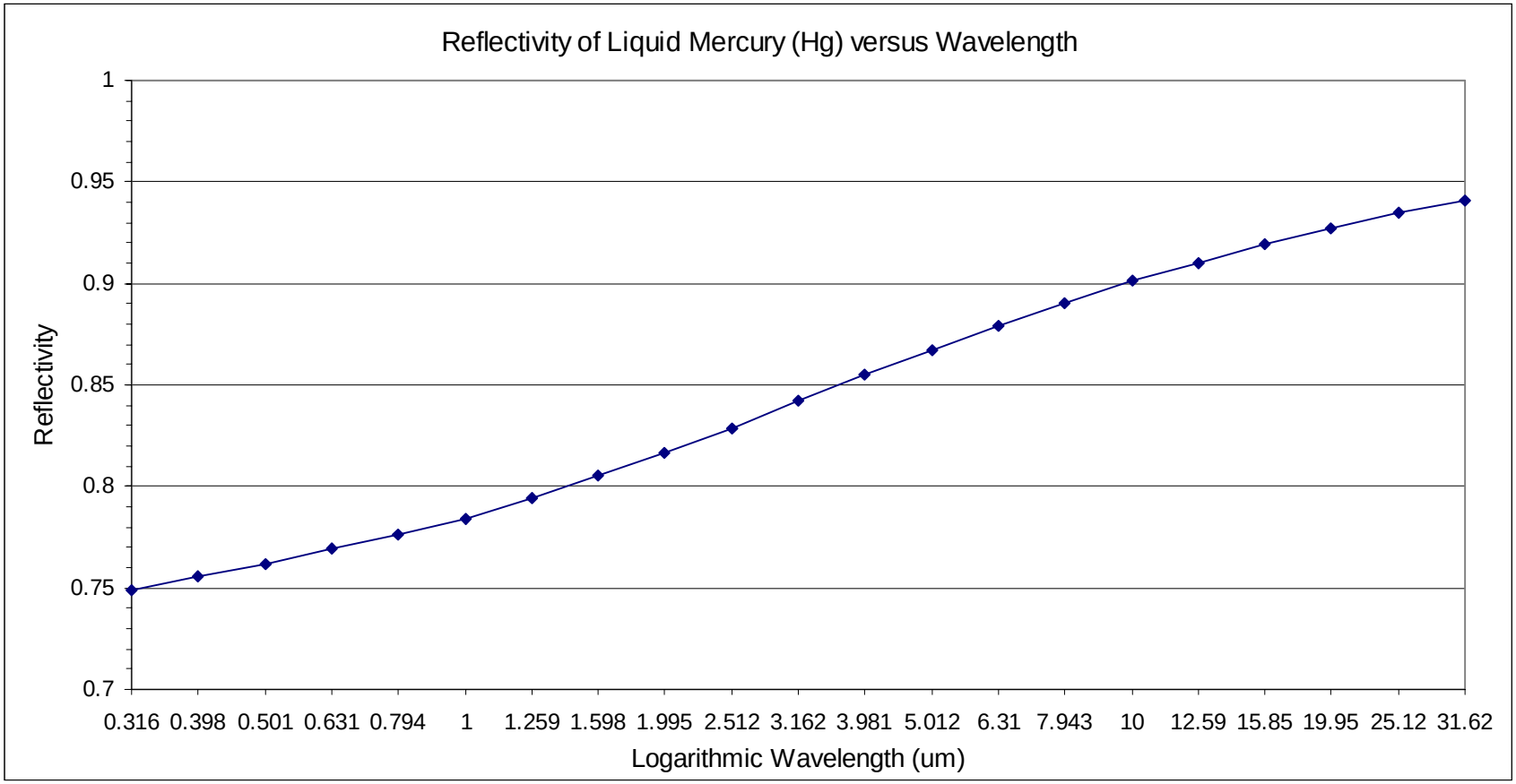

Figure IV.H-1 A graph demonstrating the reflectivity of liquid mercury (Hg) at various optical and infrared wavelengths. The average reflectivity in the optical range (400-900 nm) is 76.5%. Although a freshly aluminized or silvered glass surface can have a reflectance of 98%, that performance is rarely realized consistently because the coating degrades and recoating is expensive and laborious. A liquid mirror can be cleaned daily or weekly if necessary and thus a constant reflectivity maintained. At mid-infrared wavelengths, the Hg reflectivity improves substantially. The NASA-LMT is currently (2000) undergoing modifications to enable use of an infrared detector. Data courtesy Paul Hickson.

complication is introduced of adding an additional transparent over-coating layer to the Gallium. Rubidium and Cesium are also liquid metals at room temperature, but they expensive, have poor reflectivity and are highly chemically reactive.

Mercury, whether in elemental form, as an inorganic salt, or organic compound, can be absorbed by biological systems where it can affect the central nervous system (CNS), kidneys, liver, and other organs and tissues (Casarett and Doull 1983). Elemental mercury utilized in LMTs is primarily assimilated via inhalation of its vapors whereby it is absorbed by red blood cells and transported throughout the body. Fortunately, ingestion or physical contact with elemental mercury does not pose a significant threat since it is not readily absorbed through the skin or the gastrointestinal (GI) tract. Mercury salts or organic compounds conversely are readily absorbed via the GI tract and are therefore generally associated with mercury related poisoning and death. The organic properties of methylated mercury make it particularly harmful wherein 90 and 95 percent of that ingested is absorbed versus only 0.01 percent of the elemental form. The tragic epidemics of mercury poisoning in Japan during the 1950s and 1960s were due to methyl mercury which had concentrated in fish and shellfish living in oceanic waters contaminated with industrial effluent. A similar epidemic in Iraq in 1971, which killed 500 people, was due to ingestion of wheat treated with a methyl mercury fungicide. With regard to mercury salts, the term ”mad as a hatter” derives from those afflicted with poisoning from mercury nitrate which was once used to soften fur in the manufacture of felt for hats.

Although generally not associated with acute poisoning or death, the long-term inhalation of elemental Hg vapor can produce chronic health effects which include

muscle tremors, loss of fine motor skills, memory loss, hallucinations, and personality changes. At NODO, extensive measures have been taken to protect and monitor employee health, to protect the facility from contamination, and to quantify Hg vapor emissions.

Employee protection is ensured by following the guidelines set by the Occupational Safety and Heath Administration (OSHA) for the maximum allowable Hg vapor concentration when using various forms of respiratory protection. Half-mask respirators utilizing sulfur impregnated activated carbon disposable cartridges must be worn if the vapor concentration exceeds 25 $microgram(\mu g)/m^3$ and a supplied-air respirator is required if the vapor concentration exceeds $500\,\mu g/m^3$, (although the latter condition has never been encountered at NODO). Employees must wear protective suits and gloves when handling mercury, and are given both a complete physical evaluation and tested specifically for Hg contamination on an annual basis. No anomalies have been detected after seven years of cumulative exposure to liquid mercury and its vapors via NASA-JSC and NODO operations.

To protect the facility, the area around the mirror is sealed with epoxy and the pier itself contains four sealed channels that could contain the volume of mercury in the mirror in the event of a catastrophic failure of the mirror container. In the event a small spill occurs, such as when mercury is added or removed from the mirror, a mercury vacuum cleaner manufactured by Hako is available for clean-up. Since the entire area is sealed, with time and perseverance all Hg can be recovered. The vacuum cleaner, shown in Figure IV.H-2, is also used to remove small pieces of debris during mirror start-up as

NASA-LMT @ NODO: Hako Mercury Vacuum Cleaner

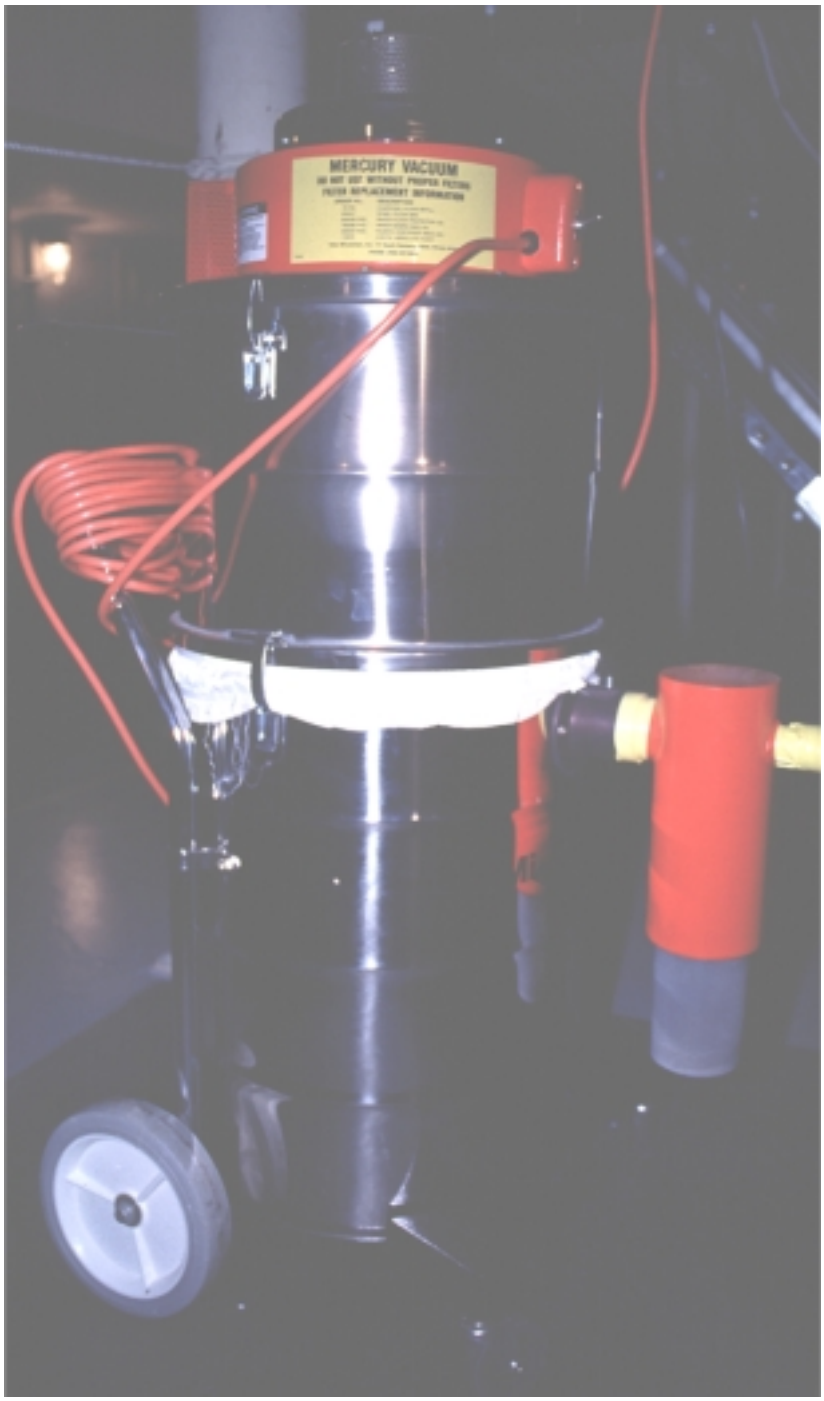

Figure IV.H-2. The Hako Mercury vacuum cleaner utilized to remove debris during mirror cleaning operations, or to recover Hg if a spill occurs. The clear reservoir at left retains bulk Hg which can later be filtered and reclaimed. Mercury vapor is trapped via internal activated carbon and HEPA (High Efficiency Particulate Arresting) filters. The vacuum is stationed adjacent to the pier at NODO.

described in Chapter V. The portion of recovered Hg which cannot be filtered and reclaimed is treated as hazardous waste and disposed of commercially. Elemental Hg released into the environment can become methylated by bacteria in lakes and streams.

When it is necessary to add or remove mercury to or from the mirror, a peristaltic pump is used to access a Stainless Steel (SS) reservoir that contains several liters of reserve mercury and is located beneath the mirror. By using a peristaltic pump, the Hg only contacts a Neoprene hose rather than contaminating a pump mechanism. Hg is occasionally added to replace the small amounts removed via the cleaning process described in Chapter V. Similarly, Hg may be removed to test thinner layers (Hg is extricated via a tube inserted in the mirror's central hub), or the mirror may be emptied completely if major modifications to the mirror subsystem are required, such as work on the drive motor or base. The peristaltic pump and containment reservoir as well as a demonstration of the addition of Hg to the mirror are shown in Figures IV.H-3 and 4.

The mirror and storage reservoir contain triple-distilled scientific grade mercury. The mercury was first poured into the reservoir from 500 ml plastic containers prior to being pumped into the mirror. During the pouring process, it was immediately evident that Hg should be poured from a minimal height, otherwise the falling stream of high density fluid impacts with great force (even from a few centimeters height) and the kinetic energy dissipated yields many small Hg droplets as ejecta which were easily able to exit the 43 cm deep container.

In an effort to quantify the hazard posed by the liquid mirror in various environments, extensive monitoring has been performed at JSC and NODO of Hg vapor

NASA-LMT @ NODO: Peristaltic Pump and Hg Reservoir

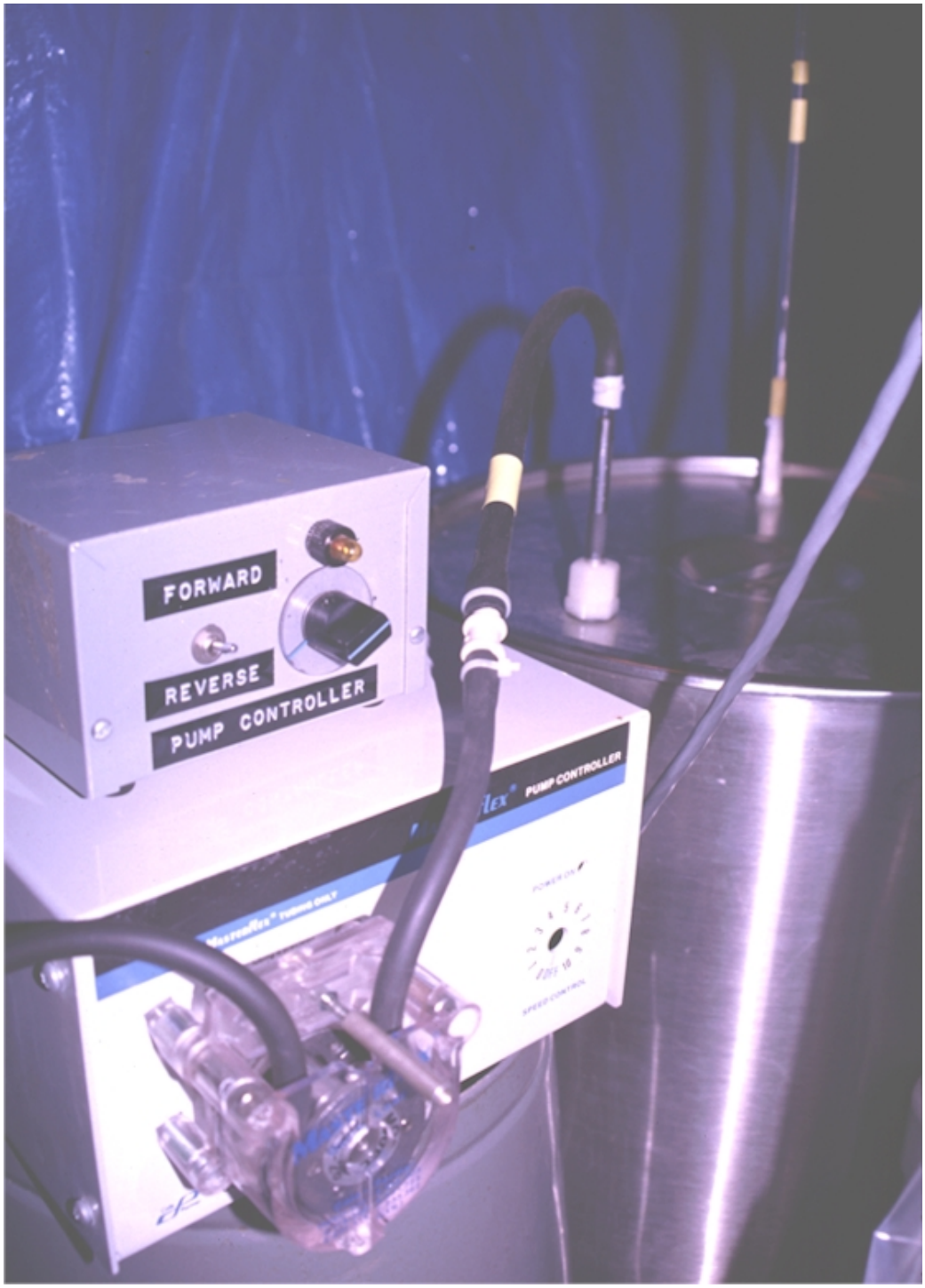

Figure IV.H-3. The Stainless Steel Hg Reservoir and peristaltic pump used for adding and removing Hg from the liquid mirror. Mercury is moved through the Neoprene tubing via peristalsis thereby eliminating Hg contamination of a pumping mechanism. A calibrated float level in the reservoir indicates the volume of Hg removed or returned.

NASA-LMT @ NODO: Adding Hg to the Liquid Mirror via the Peristaltic Pump

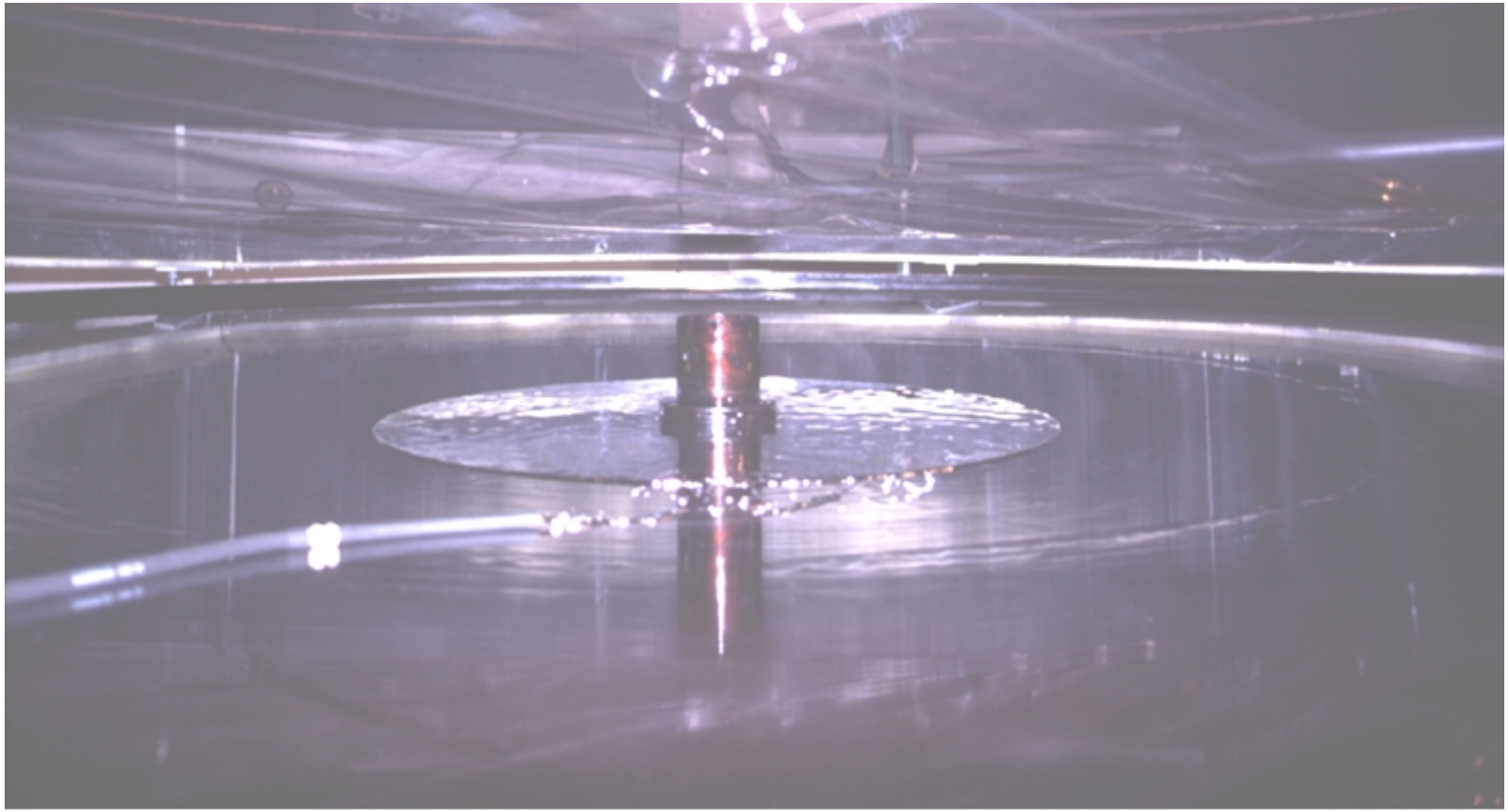

Figure IV.H-4. Demonstration of the addition of Hg to the NASA-LMT mirror container. The mercury is extracted from a reservoir by a peristaltic pump and deposited via a Neoprene tube onto the mirror container.

concentrations at a distance of between 4 and 5 meters from the center of the NASA liquid mirror. These measurements have been acquired at a wide range of temperatures during all phases of LMT operations, including mirror cleaning and start-up, normal astronomical or orbital object data acquisition, and mirror shutdown. A Hg vapor concentration sensor and data logger manufactured by Arizona Instruments (Figure IV.H-5) were used to acquire the vapor samples. The instrument acquires periodic air sample and passes them over a gold film. A portion of the Hg vapor in the sample amalgamates with the gold and alters its resistivity. By measuring the film resistance, the Hg vapor concentration can be ascertained.

Two samples of the raw vapor concentration data from the JSC location are shown in Figures IV.H-6 and 7. The data were acquired under the high temperature (24-38 ^{0}C) and relative humidity (85-100%) conditions typical of Houston, TX. Each trace covers both the cleaning and start-up of the mirror and 3.6 and 4 days respectively of operations including nightly data acquisition. Data acquisition involves opening the roof of the facility, consequently promoting ventilation and temporarily reducing Hg vapor concentrations. The vapor concentrations are initially very high, even requiring use of a self-contained respirator in the first example. They then decline slowly with the diurnal variation from solar heating clearly evident. Even at the end of each trace, average vapor concentrations significantly exceed the OSHA 25 $\mu g / m^3$ guideline indicated by the horizontal pink line.

Figures IV.H-8 and 9 show exponential fits and coefficient of determination

NASA-LMT @ NODO: Hg Vapor Concentration Sensor and Data Recorder

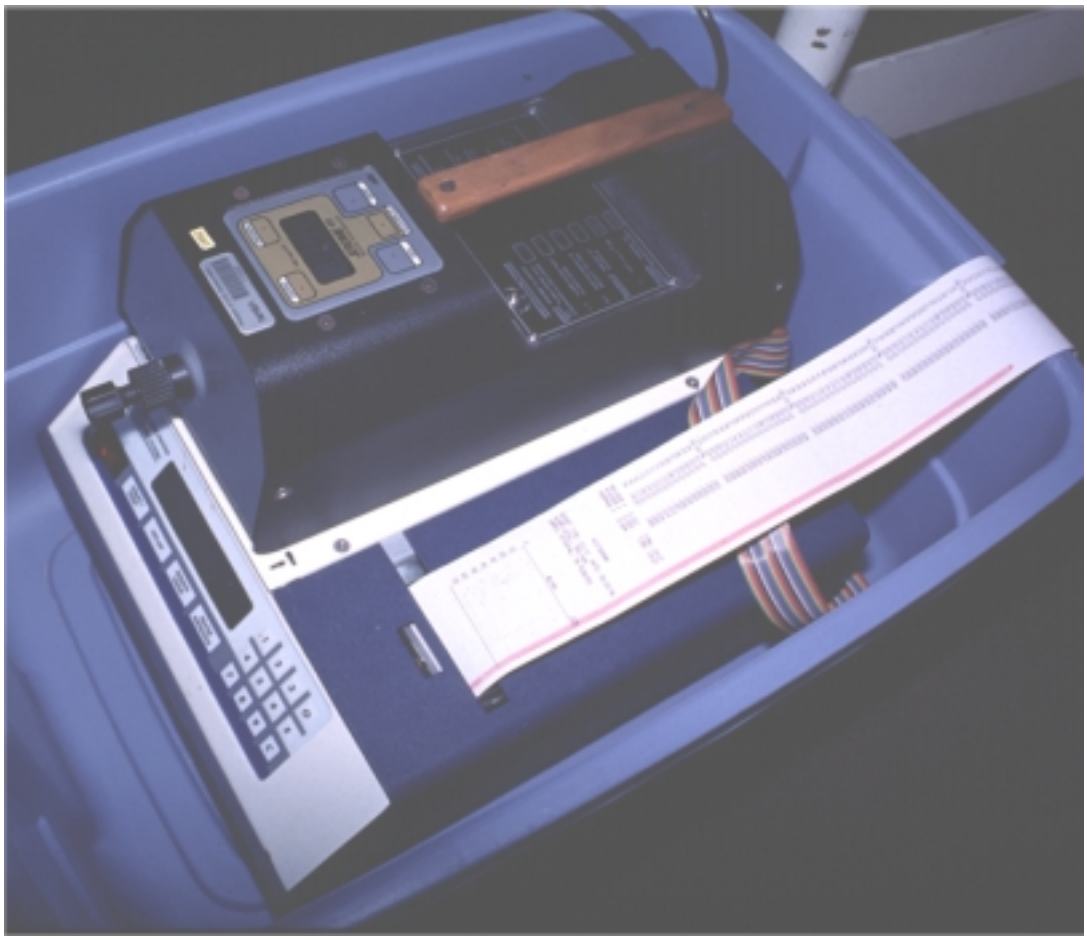

Figure IV.H-5. View of the mercury vapor sensor and data recorder used to monitor Hg vapor concentrations at JSC and NODO. Hg amalgamates with a gold film within the sensor, altering its resistivity in relation to the Hg vapor concentration. The sensor can be periodically regenerated by heating to liberate adsorbed Hg. Data samples are normally acquired 4 to 5 meters from the center of the mirror every 30 to 100 minutes year round.

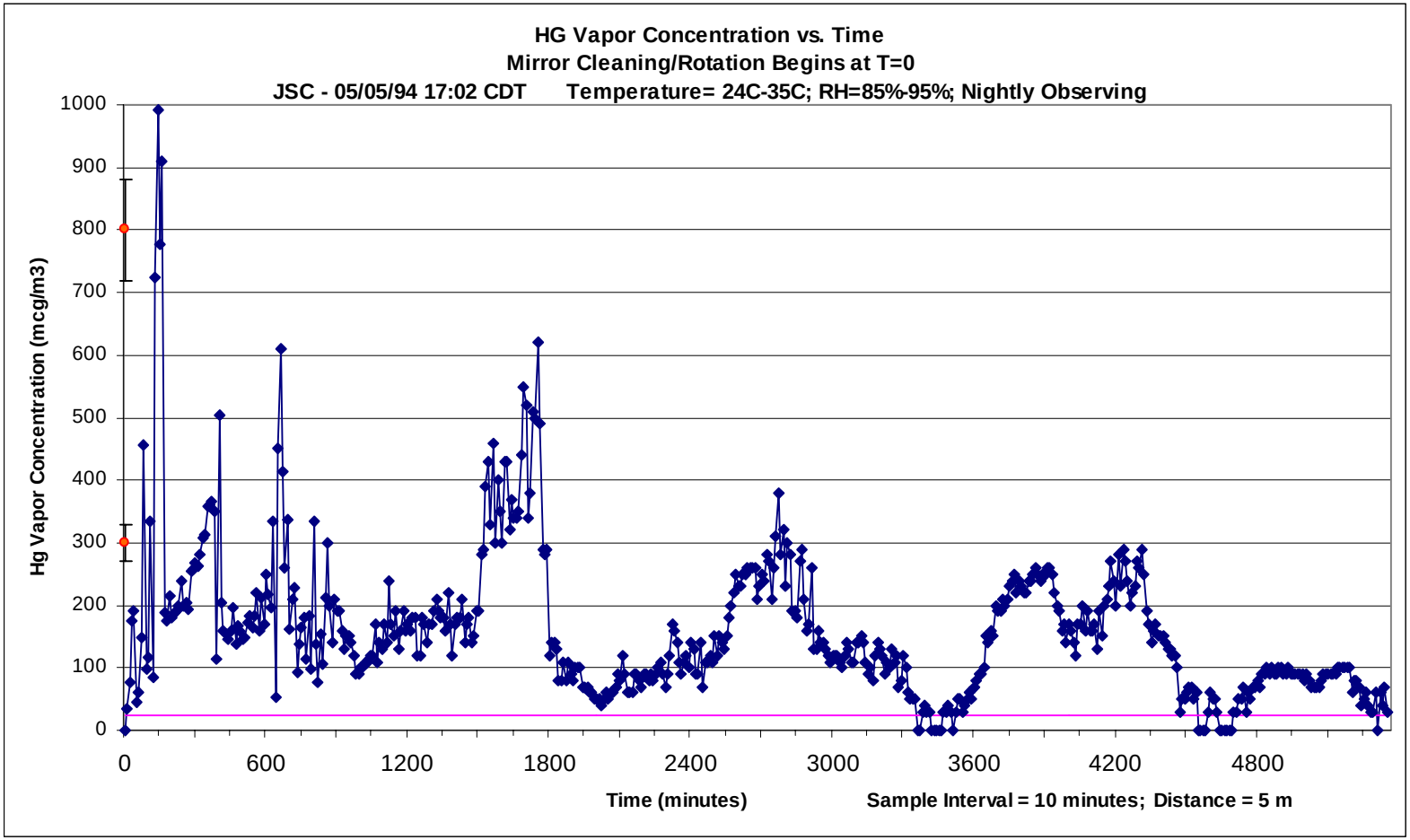

Figure IV.H-6. Hg Vapor concentration as a function of time for the NASA liquid mirror at JSC. Levels rise at the onset of mirror cleaning (T=150 min) and continue to rise to extreme levels (~1000 $\mu g / m^3$) after the mirror is formed. Levels decrease ~ 3 hrs after mirror formation as the Hg oxidizes, but even after 86 hrs (3.6 days) levels are typically well above OSHA limits (pink line). Diurnally induced temperature variations and nightly silo opening give rise to oscillations in the Hg vapor levels as they decline (~24 hr period). Error bars in red = +/-10%.

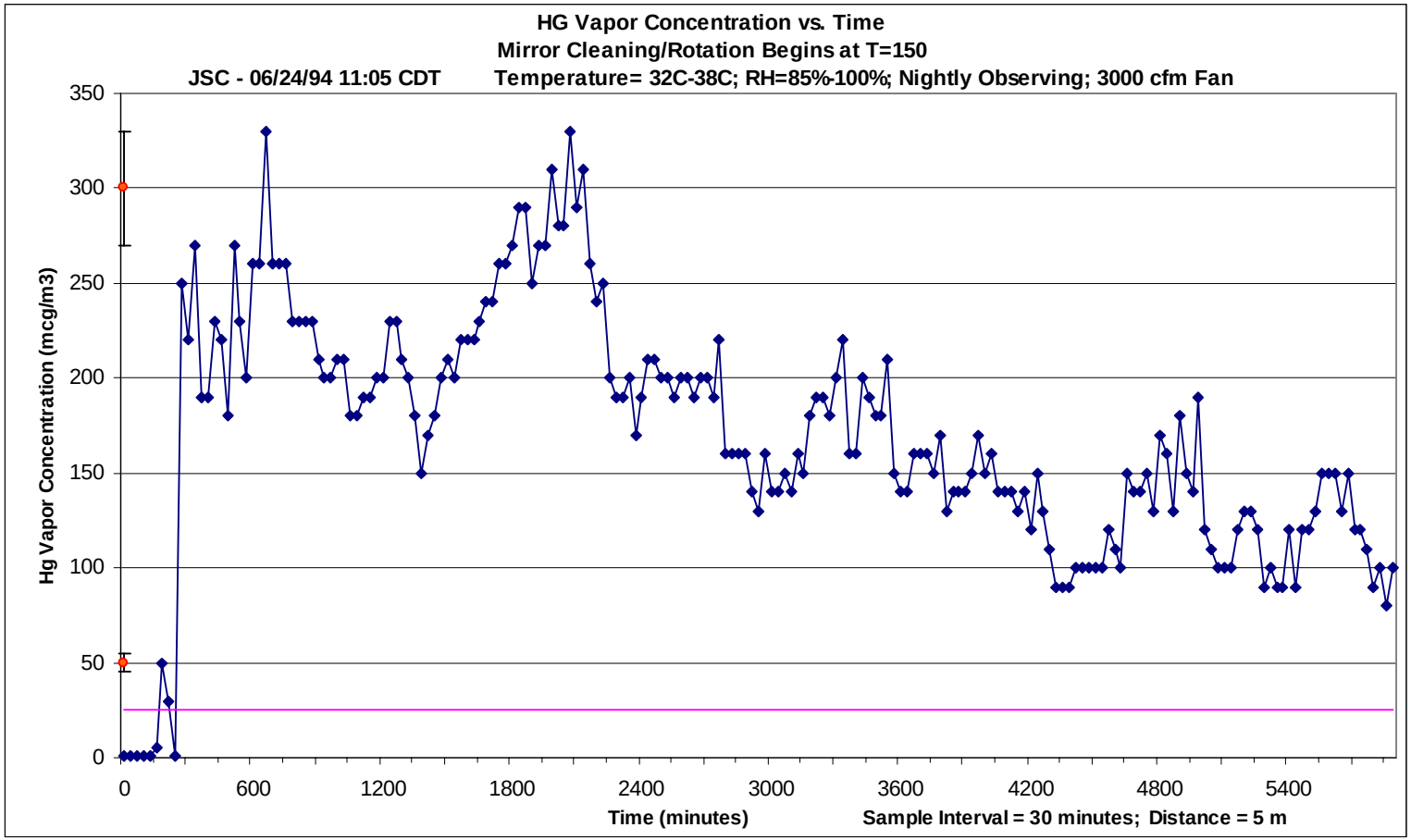

Figure IV.H-7. Hg Vapor concentration versus time for the NASA liquid mirror at JSC with a 3000 cfm ventilation fan engaged. Levels rise at the onset of mirror cleaning (T=150 minutes) and continue to a level of ~300 $\mu g / m^3$ after the mirror is initially formed. Levels begin to decrease ~5 hrs after mirror formation, as the Hg oxidizes. Diurnally induced temperature variations and nightly silo opening give rise to oscillations in the Hg vapor levels as they decline (~24 hr period). After 3.8 days vapor levels are still well above OSHA limits (pink line). Error bars in red = +/-10%.

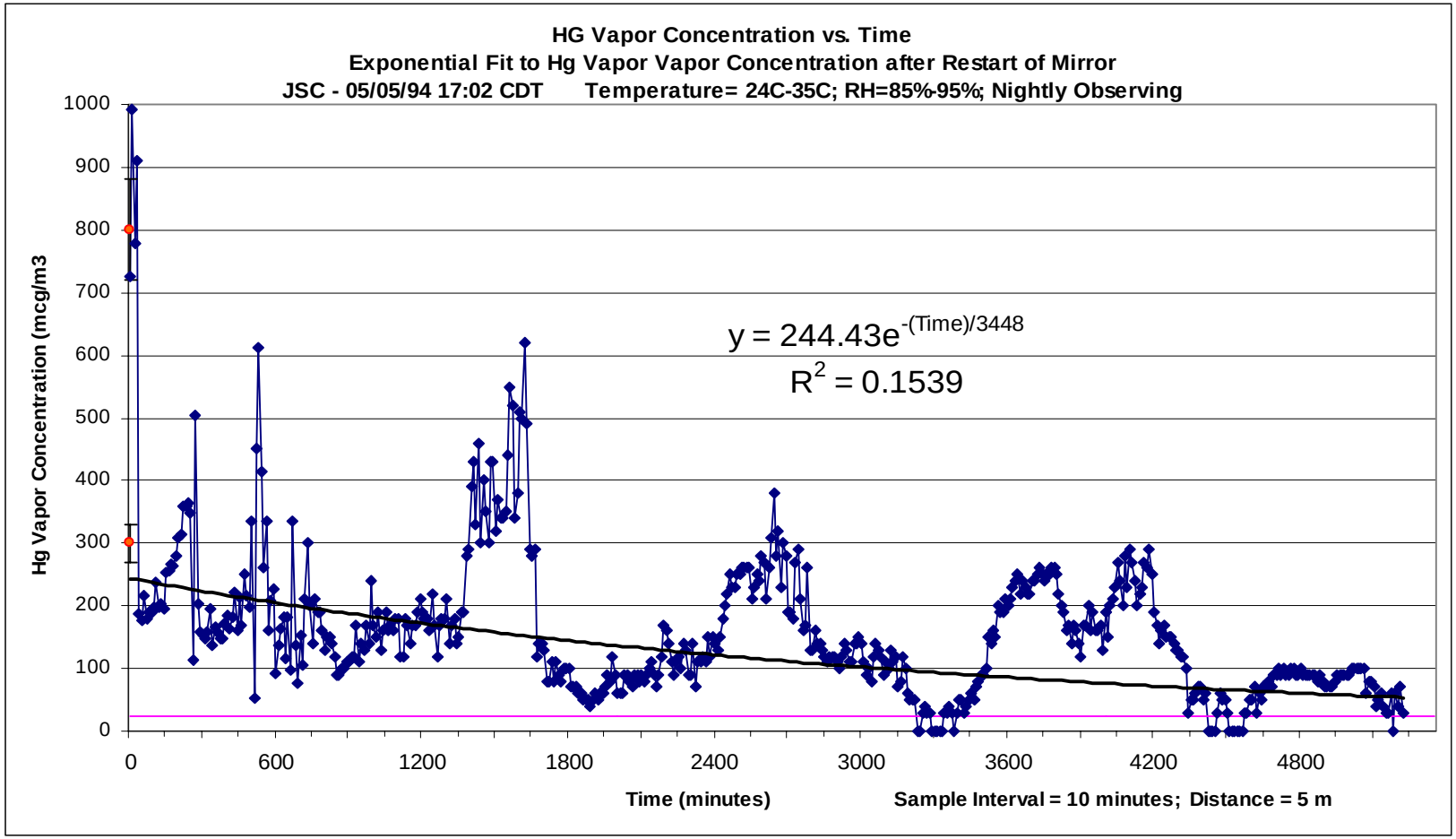

Figure IV.H-8. An exponential curve fit to the Hg Vapor concentration as a function of time for the NASA liquid mirror at the JSC location. The trend-line is for data acquired after the mirror is formed. The time constant for the decay is 3448 minutes (2.4 days). Because of the high initial concentrations, the levels would not decay permanently to the OSHA 25 $\mu g / m^3$ safe level (pink horizontal line) for more than 5 days.

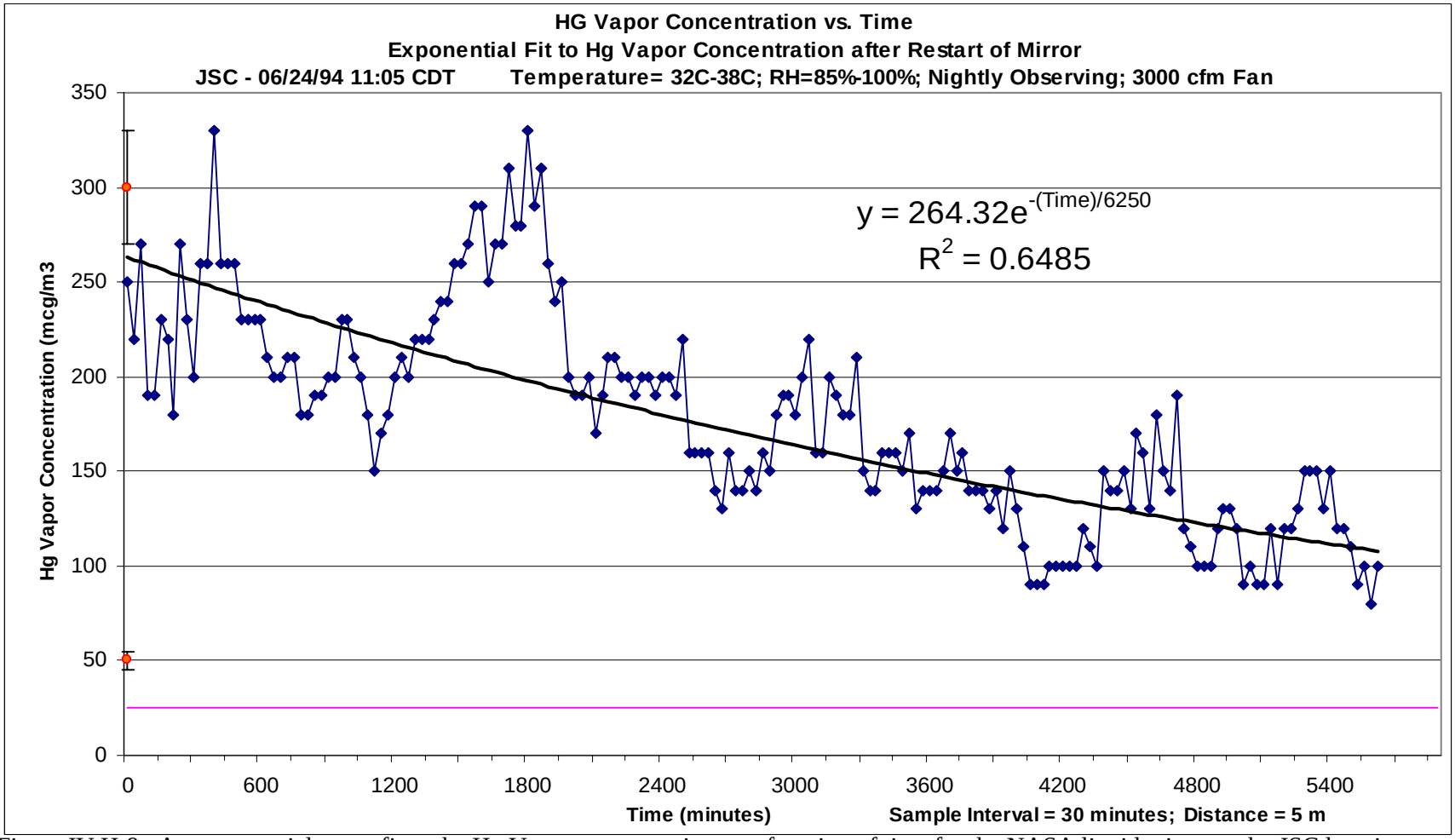

Figure IV.H-9. An exponential curve fit to the Hg Vapor concentration as a function of time for the NASA liquid mirror at the JSC location. The trend-line is for data acquired after the mirror is formed. The time constant for the decay is 6250 minutes (4.34 days). Because of the high initial concentrations, the levels would not decay permanently to the OSHA safe level (pink horizontal line) for more than 9 days.

values (R^2) for each JSC data set, beginning after the cleaning process has ended. The exponential decline in Hg vapor concentration is attributed to oxidation of the mercury surface and has been observed with other liquid mirrors (Borra 1985b). The oxide forms as a transparent, rigid sheet covering the entire mirror as ascertained during the cleaning process described in Chapter V. Acting as a membrane, it may help damp surface waves, but this has not been verified. The time constants for the exponential decay are 3448 minutes (2.4 days) and 6250 minutes (4.34 days) respectively. Because of the high initial Hg concentrations, the levels indicated by the trend-lines would not fall to safe (respirator not required) levels for approximately 5 and 8.5 days respectively. But because of the wide variations about these trends, levels would not be permanently below the OSHA 25 $\mu g / m^3$ limit for several days beyond this. If the mirror is cleaned weekly, a respirator would be required at all times at the JSC location.

A very different situation is encountered at NODO where respiratory protection is normally required only during the cleaning process and the subsequent 24 to 48 hour period. Figures IV.H-10 and 17 show Hg vapor concentration data were acquired under the normally low to moderate temperature (0-20 ^0C) and relative (30-50%) humidity conditions typical of Cloudcroft, NM. Figures IV.H-10 and 11 cover the entire process of mirror-shutdown, mirror cleaning, mirror startup, and post-startup (mercury surface oxidation) for several days. The mirror-shutdown process is characterized by a rapid diminution in the Hg vapor concentration presumably because the oxide sheet collapses and thickens over the Hg surface when the mirror rotation is halted. This collapsed oxide

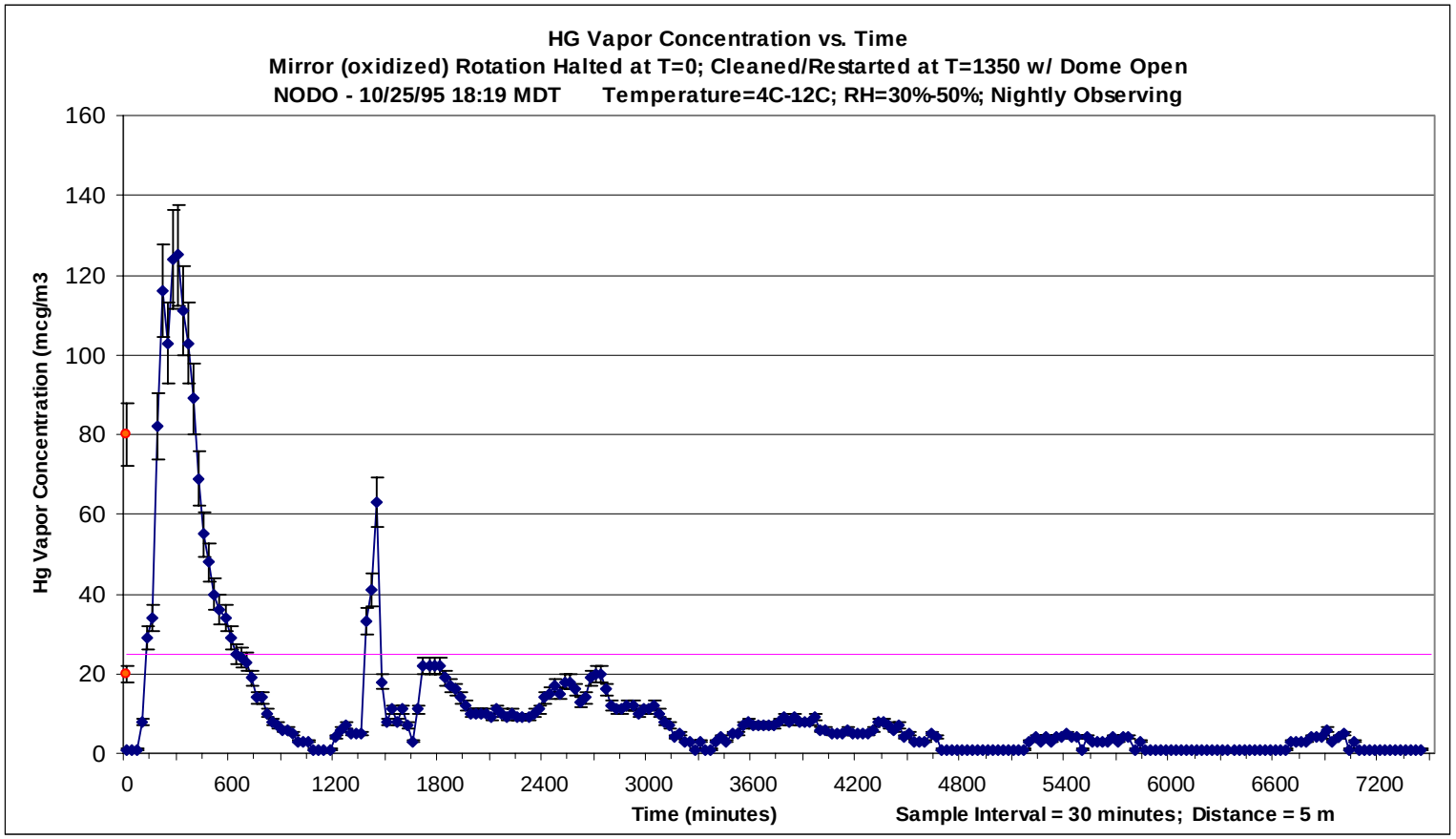

Figure IV.H-10. Hg Vapor concentration as a function of time for the NASA liquid mirror at NODO . The initial transient (T=100 minutes) results when rotation of the fully oxidized mirror is halted. Hg vapor levels rise when the Hg surface is disturbed, then decrease rapidly as the pre-existing oxide layer inhibits evaporation from the collapsed Hg pool. With the dome open the mirror is cleaned and reformed at Time=1350 minutes. Levels rise only slightly at the onset of mirror cleaning and continue to rise modestly after the mirror is formed. Levels then rapidly decrease 2.5 hrs after mirror formation as the Hg surface begins to oxidize. With the dome open for a single night's observations, levels rapidly dropped below OSHA limits (pink horizontal line) and remain there even after the dome is closed. Error bars in red = +/-10%.

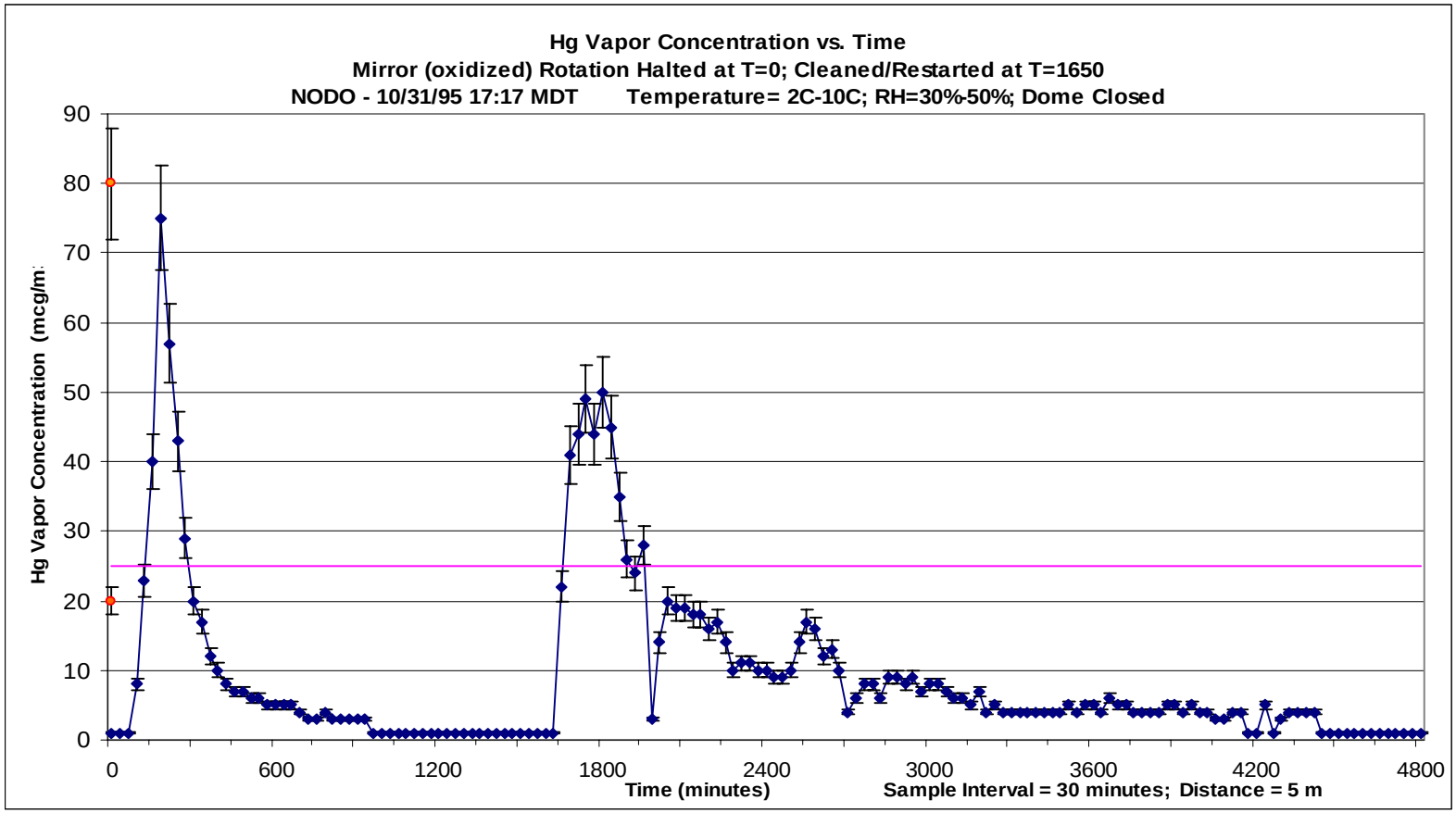

Figure IV.H-11. A graph showing Hg Vapor concentration as a function of time for the NASA liquid mirror at the NODO location. The initial transient (Time=100 minutes) results when rotation of the fully oxidized mirror is halted. Hg vapor levels rise when the Hg surface is disturbed, then decrease rapidly as the pre-existing oxide layer inhibits evaporation from the collapsed Hg pool. With the dome open the mirror is cleaned and reformed at Time=1650 min. Levels begin to rise only slightly at the onset of mirror cleaning and continue to rise modestly after the mirror is formed. Levels then rapidly decrease 4 hrs after mirror formation as the Hg surface begins to oxidize. With the dome open for a single night's observations, levels rapidly dropped below OSHA limits (pink line) and remain there even after the dome is closed. Error bars in red = +/-10%.

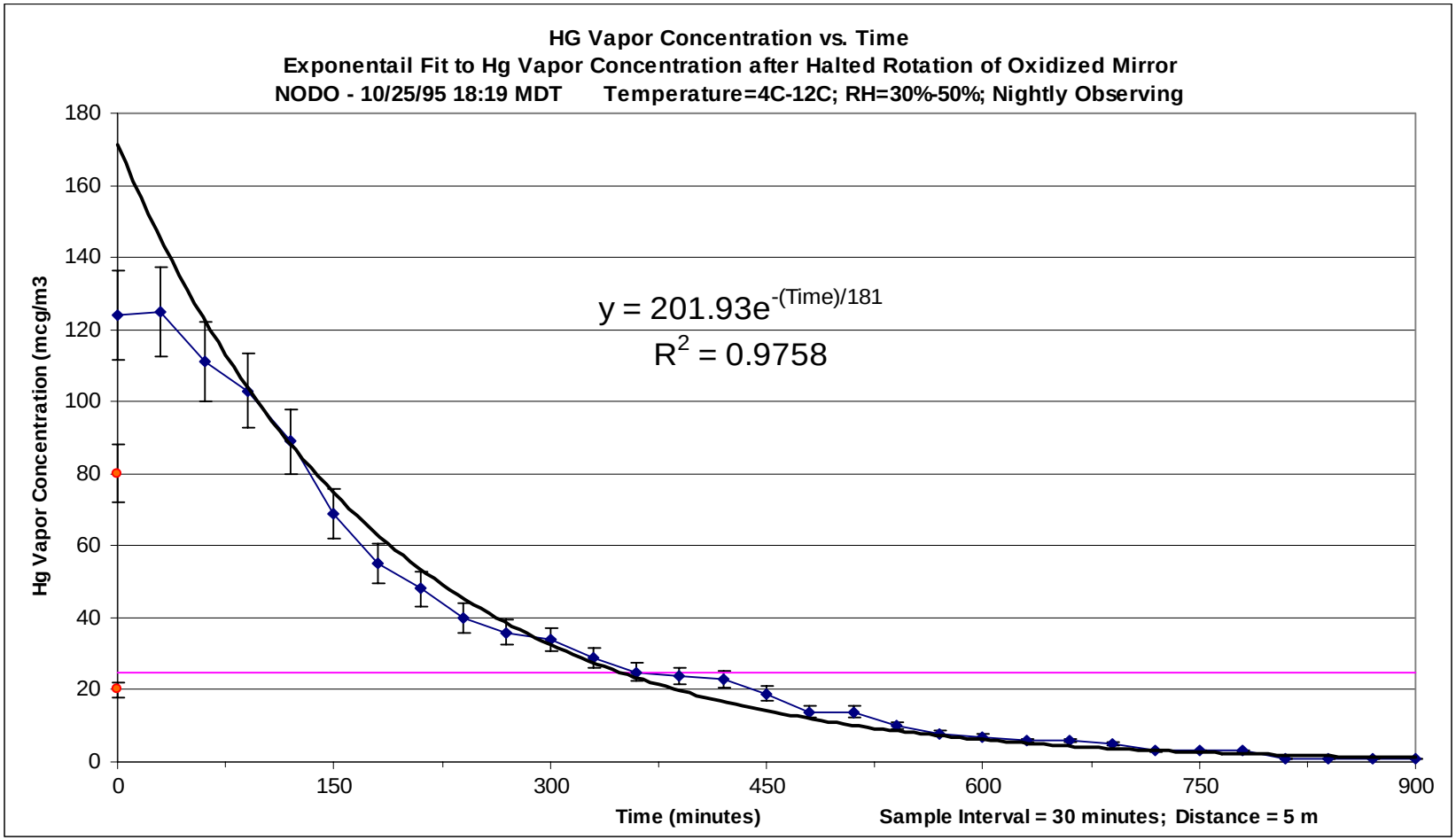

Figure IV.H-12. A graph showing Hg Vapor concentration as a function of time for the NASA liquid mirror at the NODO location. The exponential trend-line is for data acquired immediately after rotation of the oxidized mirror is halted. The time constant for the decay is 181 minutes indicating a rapid diminution in vapor concentration presumably due to the oxide sheet inhibiting evaporation from the collapsed HG pool. Levels are below the OSHA safe level of 25 $\mu g / m^3$ (pink line) within 6 hours.

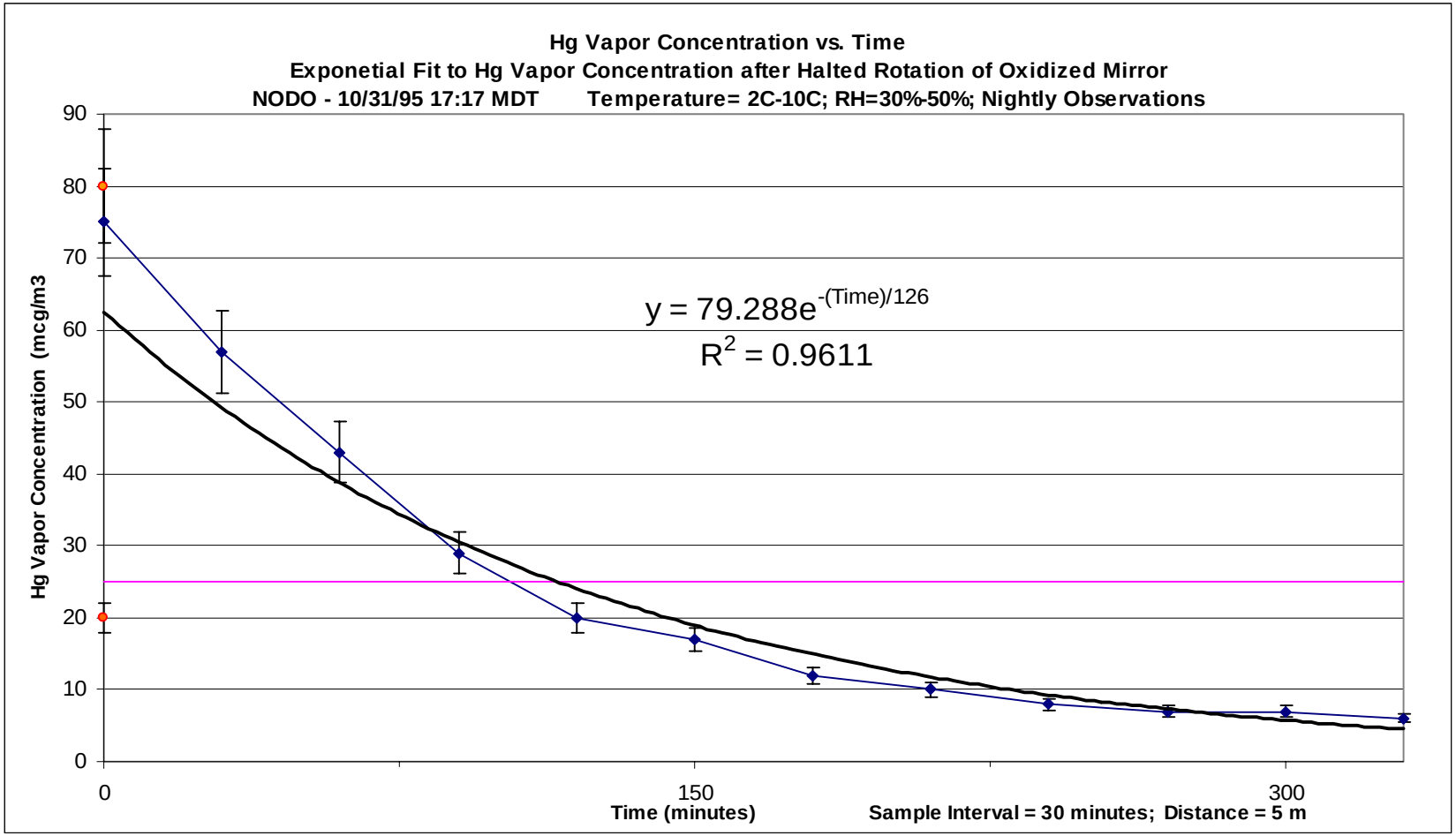

Figure IV.H-13. A graph showing Hg Vapor concentration as a function of time for the NASA liquid mirror at the NODO location. The exponential trend-line is for data acquired immediately after rotation of the oxidized mirror is halted. The time constant for the decay is 126 minutes indicating a rapid diminution in vapor concentration presumably due to the oxide sheet inhibiting evaporation from the collapsed Hg pool. Levels are below the OSHA safe level of 25 $\mu g / m^3$ (pink horizontal line) within 2 hours.

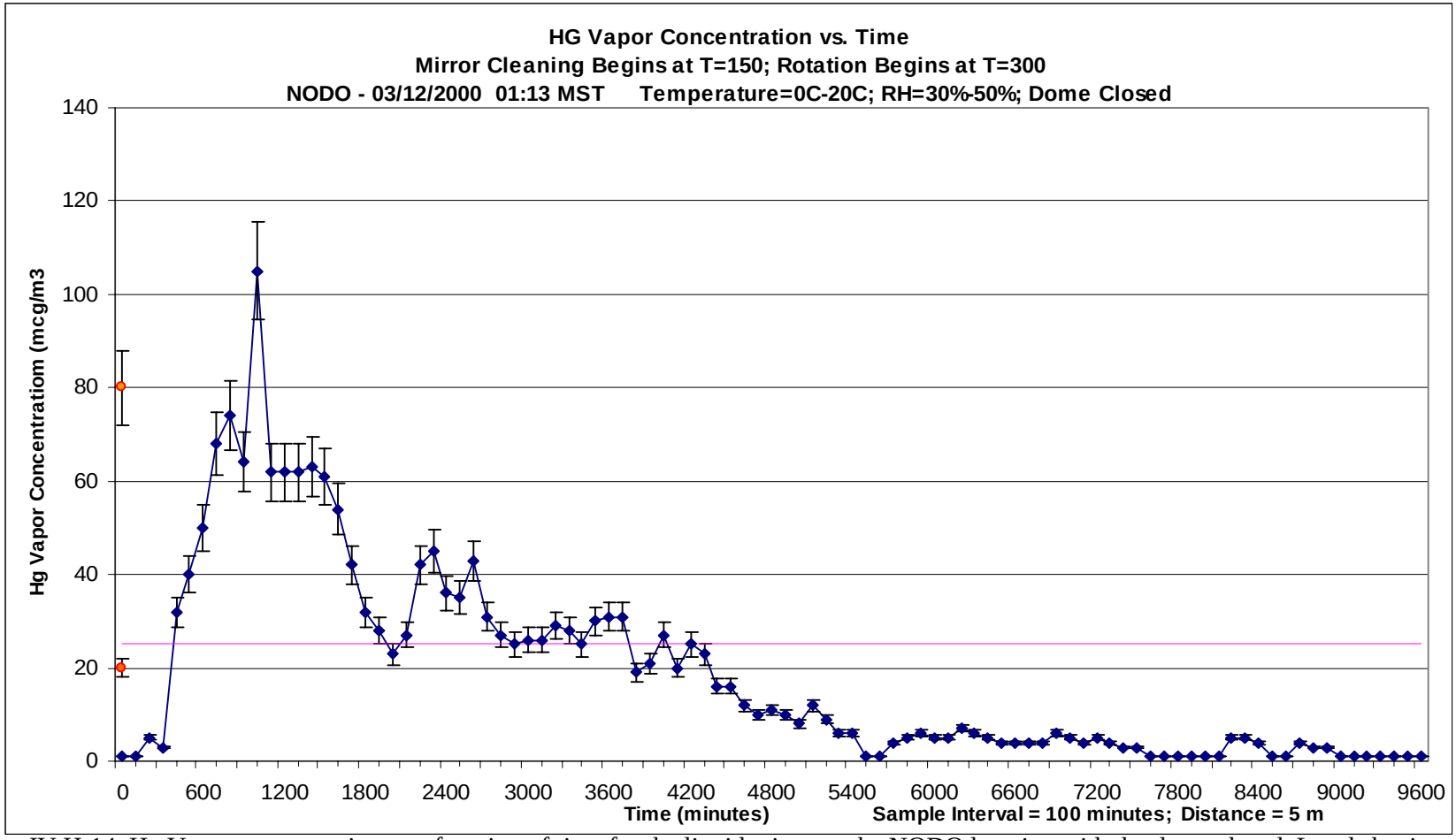

Figure IV.H-14. Hg Vapor concentration as a function of time for the liquid mirror at the NODO location with the dome closed. Levels begin to rise at the onset of mirror cleaning and continue to rise after the mirror is initially formed. Levels begin to decrease approximately 13 hrs after mirror formation as the Hg surface oxidizes. After 60 hrs (2.5 days) levels are below OSHA limits (pink line). Colder temperatures at NODO's high altitude location (2772 m) are conducive to minimizing Hg evaporation. Error bars in red = +/-10%.

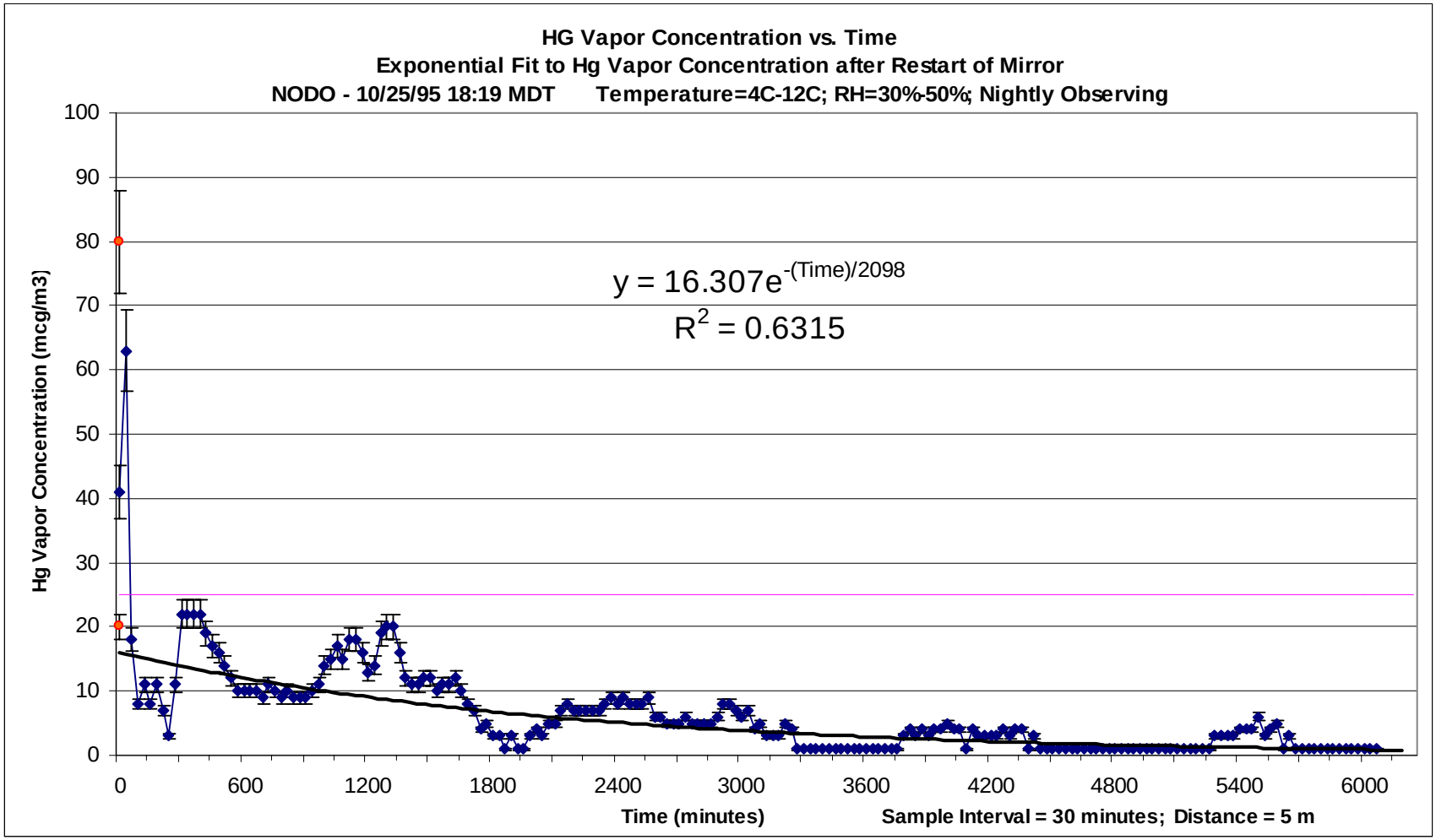

Figure IV.H-15. An exponential curve fit to the Hg Vapor concentration as a function of time for the NASA liquid mirror at the NODO location. The trend-line is for data acquired after the mirror is formed. The time constant for the decay is 2098 minutes (1.45 days). Unlike the data acquired at JSC, the Hg vapor concentration falls almost immediately below the OSHA safe level (pink line) and remains there.

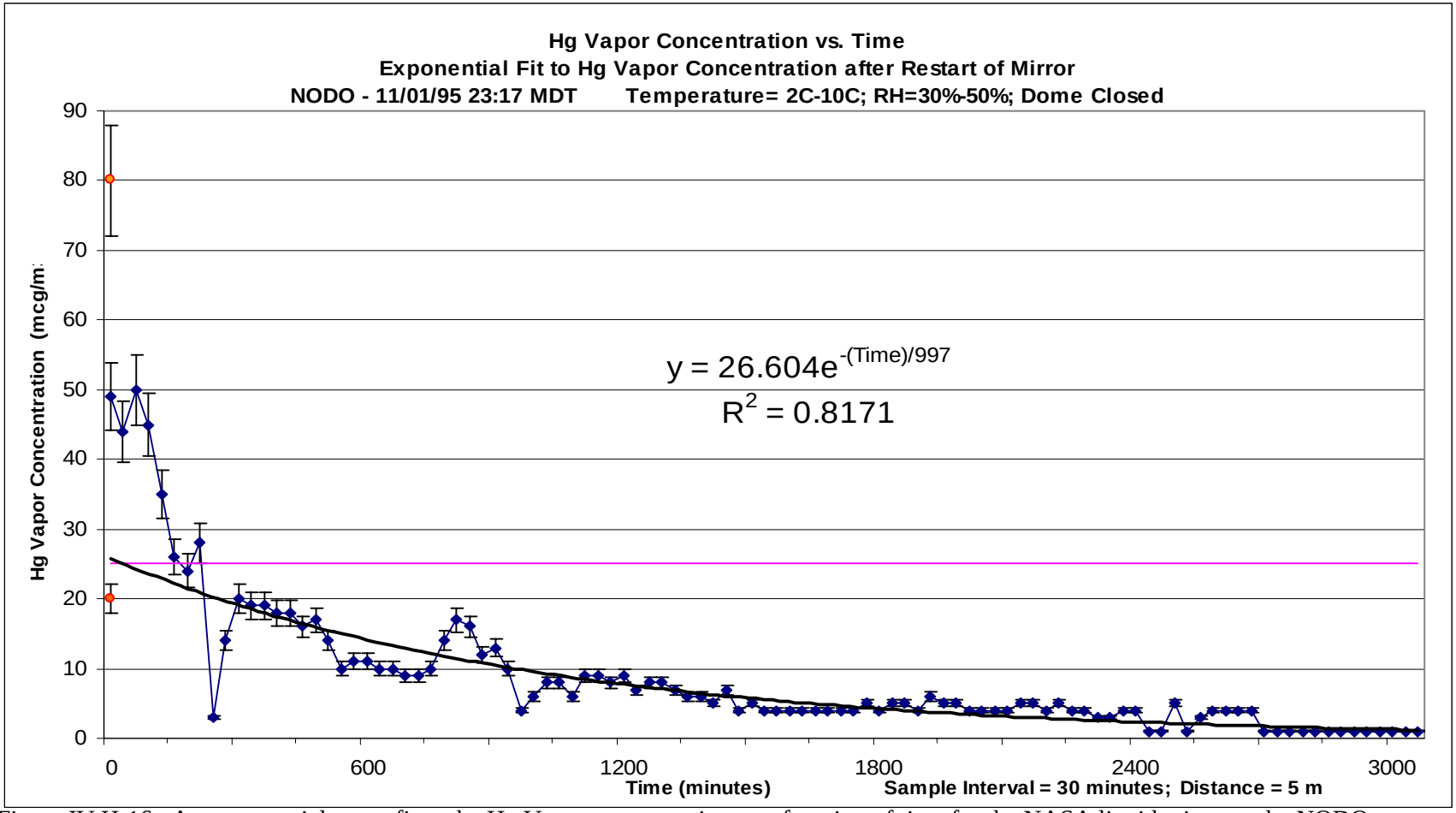

Figure IV.H-16. An exponential curve fit to the Hg Vapor concentration as a function of time for the NASA liquid mirror at the NODO location. The trend-line is for data acquired after the mirror is formed. The time constant for the decay is 997 minutes (0.69 days). Unlike the data acquired at the much warmer JSC location, within 3 hours, the Hg concentration falls below the OSHA 25 $\mu g / m^3$ safe level (pink line) and remains there.

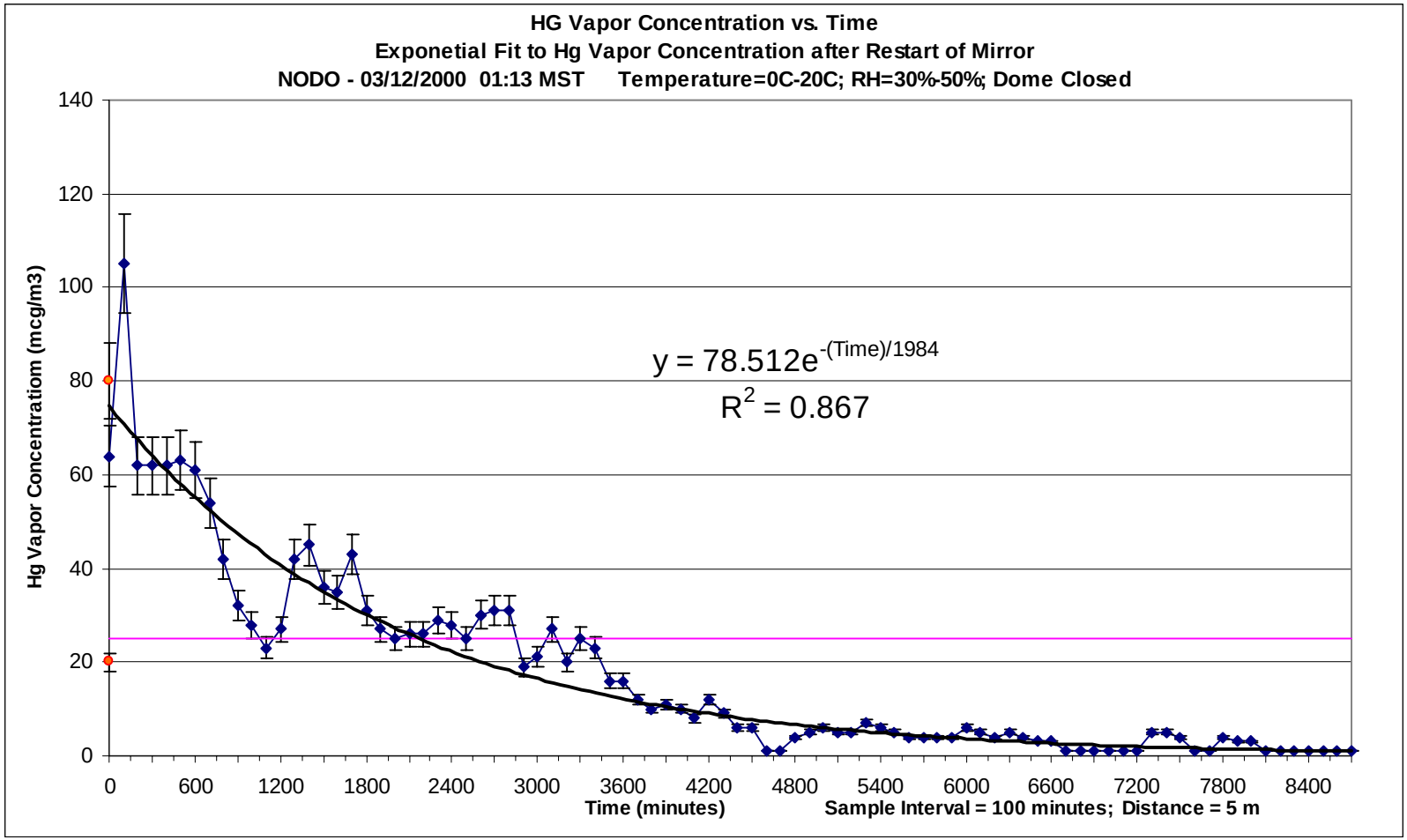

Figure IV.H-17. An exponential curve fit to the Hg Vapor concentration as a function of time for the NASA liquid mirror at the NODO location. The trend-line is for data acquired after the mirror is formed. The time constant for the decay is 1984 min (1.38 days). Unlike the data acquired at the much warmer JSC location, within 2.3 days, the Hg concentration falls below the OSHA safe level (pink line) and remains there.

sheet acts as a semi-permeable barrier to the evaporation of Hg. Compared with the mirror formation process, the characteristic time constants for the decay of the Hg vapor concentration are extremely small at 181 and 126 minutes respectively as shown in then exponential trend-lines of Figures IV.H-12 and 13. A third sample of raw Hg vapor concentration data which shows only the mirror cleaning and oxidation phases is shown in Figure IV.H-14.

Figures IV.H-15 through 17 show exponential fits and coefficient of determination values (R^2) for each of the three NODO data sets beginning after the cleaning process has ended. The exponential decline in Hg vapor concentration is similar to that observed at JSC, except the time constants and the initial concentrations are smaller, presumably due to the lower average ambient temperatures at NODO. Time constants for the NODO data vary between approximately 1000 and 2000 minutes as compared with the approximately 3500 and 6000 minute values obtained at JSC. Similarly, at NODO it is generally always safe to work near the liquid mirror without a respirator any time after a maximum of 2.5 days, whereas at JSC a vapor concentration level permanently below the OSHA 25 $\mu g / m^3$ limit was never recorded, presumably because the mirror was never left in a formed state for more than a week at a time. At NODO, it is possible to give lengthy tours of the LMT to large groups of visitors who otherwise could not view the mirror without respirator training.

From a health and safety perspective, these data emphasize the importance of locating LMTs in colder climates. At average ambient temperatures near $10^0 C$, the

OSHA 25 $\mu g / m^3$ safe level is rarely exceeded. Even at $20^0 C$, a cartridge respirator need only be worn during cleaning and the subsequent 24 to 48 hours. When the average ambient temperature exceeds 25 or $30^0 C$, however, peak Hg vapor concentration levels can require the use of a supplied air respirator, and the concentration values even after a week of oxidation can still exceed the OSHA safe standard. Above average ambient temperatures of $35^0 C$ the liquid mirror continuously represents a significant safety hazard to both workers and equipment which can be contaminated in the high Hg concentration environment. Un-anodized aluminum, for example, readily reacts with Hg vapor. The corrosion products appear as a flake-like crystalline structures. For this reasons all aluminum parts in the vicinity of the mirror are anodized. The typical high-altitude, and therefore cooler, location of astronomical observatories provides an ideal environment for LMTs.

I. Prime Focus (PF) Assembly

In order to obtain a wide field of view (FOV), the NASA-LMT was constructed as a prime focus instrument wherein the detector is located above the primary mirror at its first or primary focal point. Although parabolic mirrors are free of spherical aberration, they are subject to field curvature and off-axis aberrations of coma and astigmatism. Therefore a set of corrective optics must also be placed near the prime focus in front of the detector to reduce or remove these aberrations. Provision must also be made for

insertion of optical filters or polarizers, either individually or with a filter wheel, between the detector and corrector for photometric or polarimetric observations. To enable proper alignment of the corrector and detector both on (lateral and tilt) and along (focus) the optical axis, a set of motion stages is required for accurate remote positioning. These items together constitute the prime focus assembly which is mounted as a package on a supporting tetrapod above the NASA liquid mirror. Fundamental aspects of the elements of the prime focus assembly are discussed herein.

1) Corrective Optics

As described briefly in Chapter II, the original 3-element corrector built for the NASA-LMT was not specifically designed for drift-scanning and as such possessed severe field distortion. This caused stars passing through the FOV to move on curved trajectories at a variable angular rate resulting in various degrees of smearing of the stellar images depending on location within the field. The image degradation was most severe at the field edges where the pincushion distortion caused the greatest orthogonal motion of stellar images relative to the drift-scanning CCD which moves accumulated charge along linear columns at a constant rate. Some elongation was also noticeable at field center, despite the absence of orthogonal motion, due to the variable linear rate of stellar images - decelerating from the entry edge of the detector towards field center, then accelerating away to the exiting edge. The problem is clearly evident in trailed star images acquired by drift-scanning at a rate ~20% slower or faster than the sidereal drift. This is demonstrated

in Figure IV.I.1-1 which illustrates the curvature of stellar images across the entire 20.48 arcminute FOV of the LSP 2K CCD. The curvature is most pronounced at the field edges where the pincushion distortion is most extreme. The slight discrepancy between the curvature at the north and south edges of the FOV is due to the small-circle motion of the stars convolved with the pincushion distortion. Since the small-circle motion has a radius of curvature oriented northward, it is additive with the field distortion on the north field edge and subtractive on the south edge. The difference is apparent in Figures IV.I.1-2 and 3 which show a sidereal drift-scanned field and an enlargement of the field edges.

In the Fall of 1998, the 3rd element of the original 3-element corrector was replaced with a doublet containing an aspherical surface. This modification was made to remove the field distortion and extend the coma and astigmatism correction to cover the large FOV of the new Pixel Vision (PV) 2K CCD to be installed in late 2000. The new CCD is a 2048 pixel square array with 24 um pixels (0.960 arcsec/pixel) yielding a 60% wider field than the LSP 2K with 15 um pixels. Figure IV.I.1-4 shows a trailed drift-scan acquired with the PV 1K CCD and the modified 4-element corrector. The field distortion has been removed and only the small-circle stellar motion remains. The optical layout and spot diagram for the new corrector are shown in Figures IV.I.1-5 and 6 and the parameter file is given in Appendix C3. Performance at the field edge for the new PV 2K CCD will fall between first and second row of spots. Figure IV.I.1-7 shows the performance of the corrector in the near Infrared region should an infrared camera eventually be installed. Hickson and Richardson (1998) designed a corrector for the LZT with tilted elements which removes both field distortion and the small-circle motion of stars (Figure IV.I.1-8).

Field Distortion in the Original 3-element LMT Corrector Lens

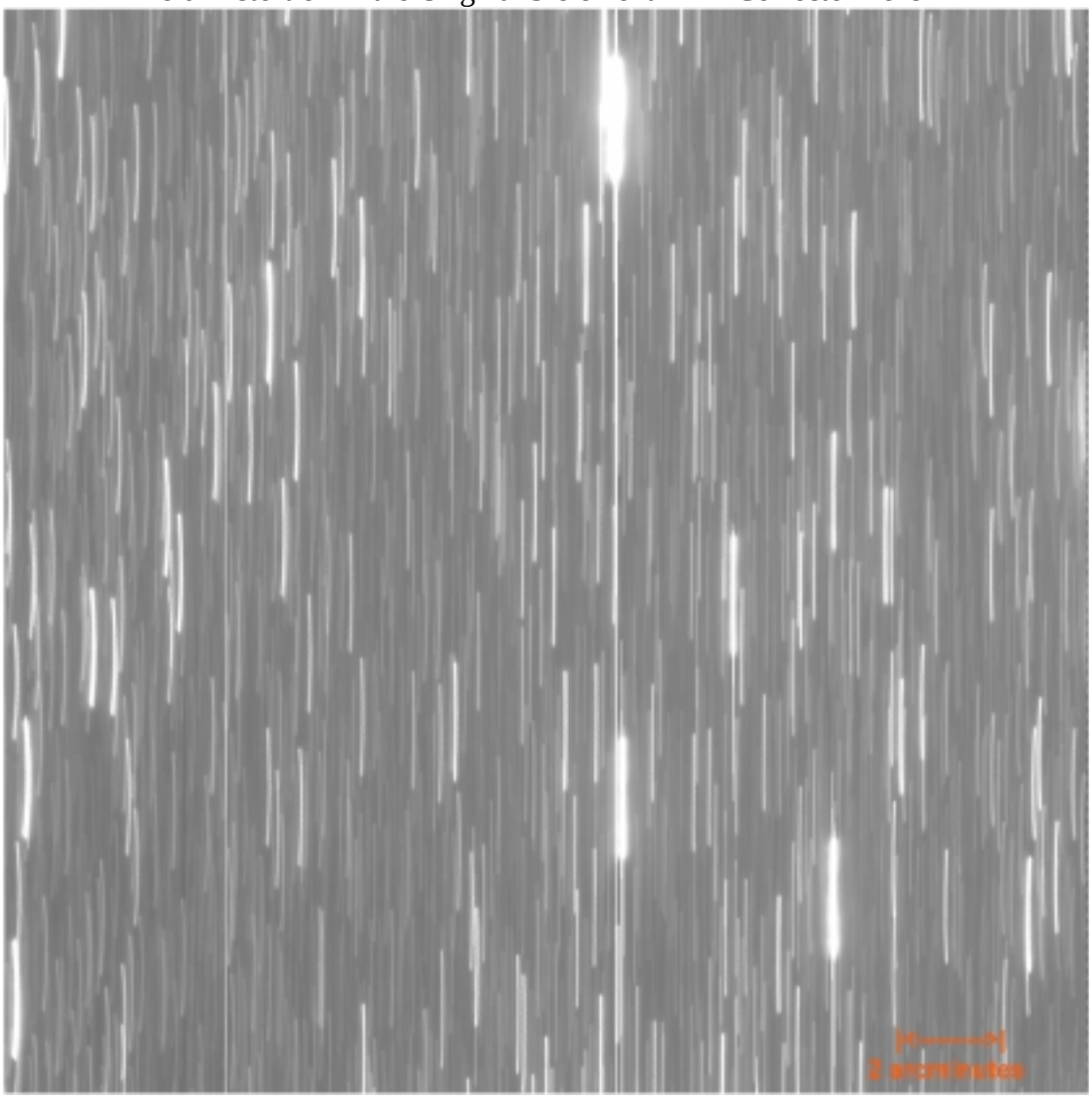

Figure IV.I.1-1. R Band trailed drift scan image of a star field within the LMT survey strip. The image was acquired with the LSP 2K CCD with a 0.600 arcsecond/pix plate scale yielding a 20.48 arcminute field of view. The pincushion field distortion is evident by the curved stellar trails whose radius of curvature is away from the field center. The distortion increases toward the field edge where it introduces a maximum 15 pixel (9.0 arcsec) lateral (N-S) variation in the path of a transiting star. This gives rise to a coma-like appearance to stars near the field edge in sidereal-rate drift scanned images. The distortion also gives rise to a longitudinal (E-W) velocity variation throughout the FOV that elongates the optimal stellar PSFs even at field center. The trailed images at the north (left) side of the FOV have more curvature than those on the south side because the small circle motion of stars (whose radius of curvature is always oriented northward for north latitudes) convolved with the field distortion, increases the curvature on the north side where the motions have similar paths and reduces the curvature on the south side where the paths are contrary and tend to cancel. In 1998 the corrector was modified to eliminate distortion by replacing the corrector rear element with an aspherical doublet. N is left, W is top.

Field Distortion in the Original 3-element LMT Corrector Lens

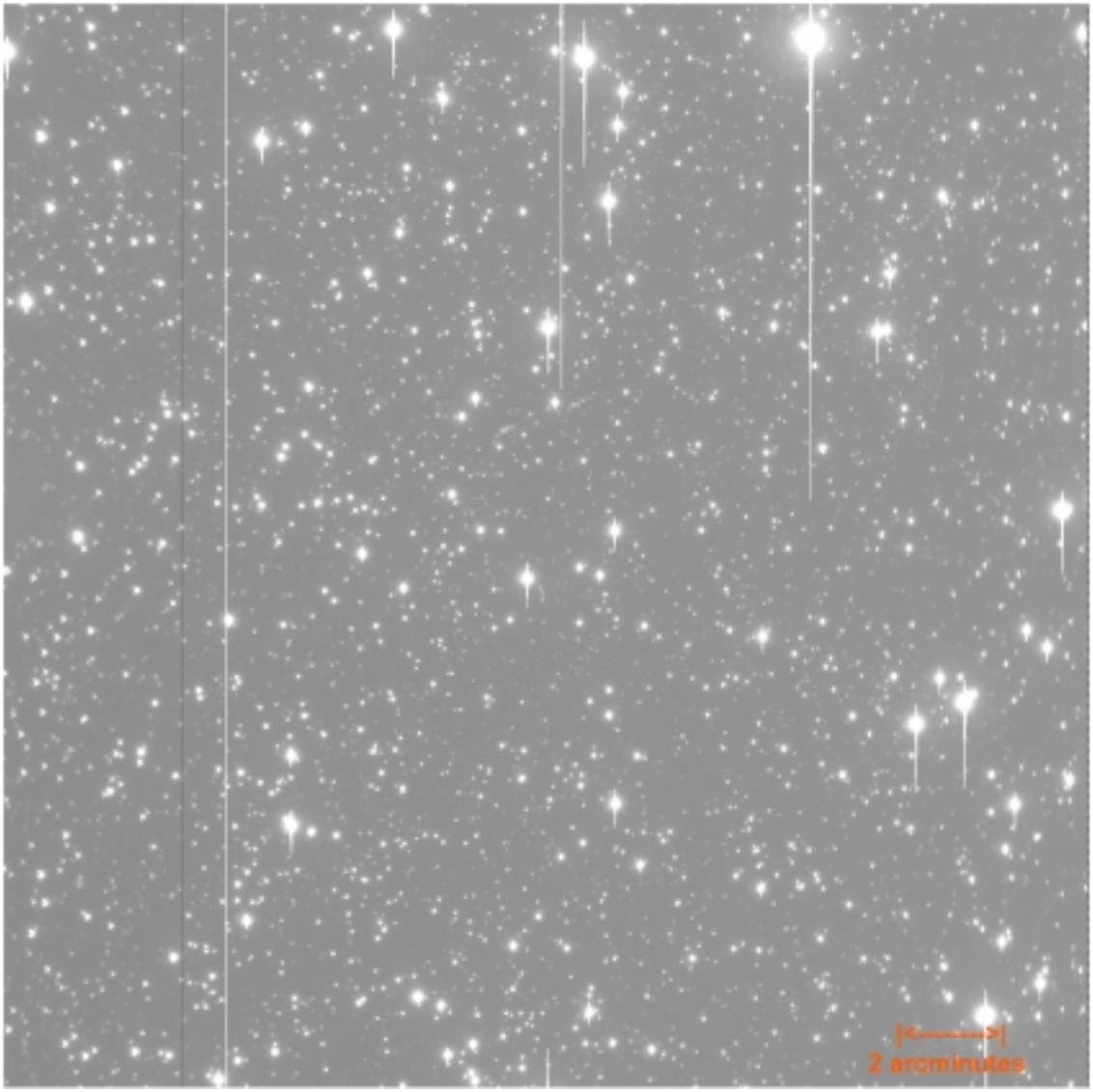

Figure IV.I.1-2. R Band sidereal drift scan image of a random star field within the LMT survey strip. The image was acquired with the LSP 2K CCD with a 0.600 arcsecond/pix plate scale yielding a 20.48 arcminute field of view. The pincushion field distortion is evident by the increasingly comatic appearance to stars away from field center. The distortion increases toward the field edge where it introduces a maximum 15 pixel (9.0 arcsecond) lateral (N-S) variation in the path of a transiting star. The distortion also gives rise to a longitudinal (E-W) velocity variation throughout the FOV that elongates the optimal stellar PSFs even at field center. The combination yields the comatic rather than astigmatic appearance to stars. The images at the north (left) side of the FOV are more distorted than those on the south side because the small circle motion of stars (whose radius of curvature is always oriented northward) convolved with the field distortion, enhances the curvature on the north side where the motions have similar paths and reduces the curvature on the south side where the paths are contrary. The next figure illustrates this effect more clearly. North is left, West is at top.

Field Distortion in the Original 3-element LMT Corrector Lens

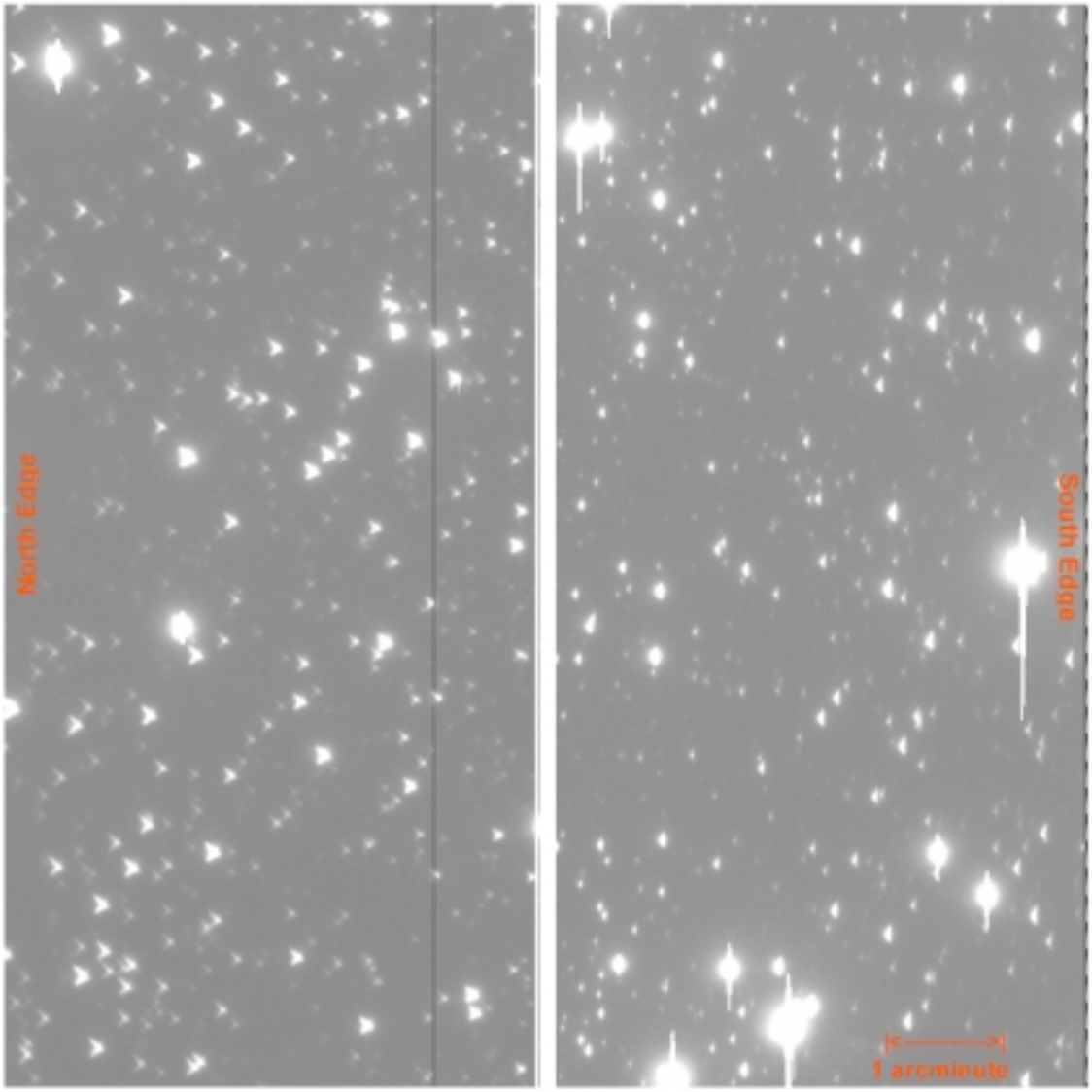

Figure IV.I.1-3. North (left) and South (right) field edges of a R Band sidereal drift scan image of a random star field within the LMT survey strip. The image was acquired with the LSP 2K CCD with a 0.600 arcsecond/pix plate scale yielding a 20.48 arcminute field of view. The pincushion field distortion is evident by the comatic appearance to stars. At the north (left) edge of the field, the distortion introduces a maximum15 pixel (9.0 arcsecond) lateral (N-S) variation in the path of a transiting star. The distortion also gives rise to a longitudinal (E-W) velocity variation throughout the FOV that elongates the optimal stellar PSFs even at field center. The combination of the two components yields the comatic rather than astigmatic appearance to stars. The images at the north side of the FOV are more distorted than those on the south side because the small circle motion of stars (whose radius of curvature is oriented northward for northern latitudes) convolved with the field distortion, enhances the curvature on the north side where the motions have similar paths and are additive and reduces the curvature on the south side where the paths are contrary and subtractive. North is left, West is at top.

Absence of Field Distortion in the 4-element LMT Corrector Lens

Figure IV.I.1-4. I Band trailed drift scan image of a random star field within the LMT survey strip. The image was acquired with the revised (4 element) LMT corrector lens and the PV 1K CCD with a 0.960 arcsecond/pix plate scale yielding a 16.38 arcminute field of view. Distortion is completely absent from the field. The small circle motion of the stars is evident by the curved nature of the stellar trails whose radius of curvature is oriented northward (left). Although not clearly evident here, the trailed images at the north side of the FOV have a smaller radius of curvature than those on the south side because they are closer to the celestial pole. Alternate corrector designs with de-centered elements can remove the small circle motion induced curvature. The field of the new corrector is virtually free from aberrations over twice the field width shown here, thus similar performance is expected with the new PV 2K CCD camera. North is left, West is at top.

Optical Layout: 4 Element Corrector for the NASA-LMT f/1.5 Primary Mirror

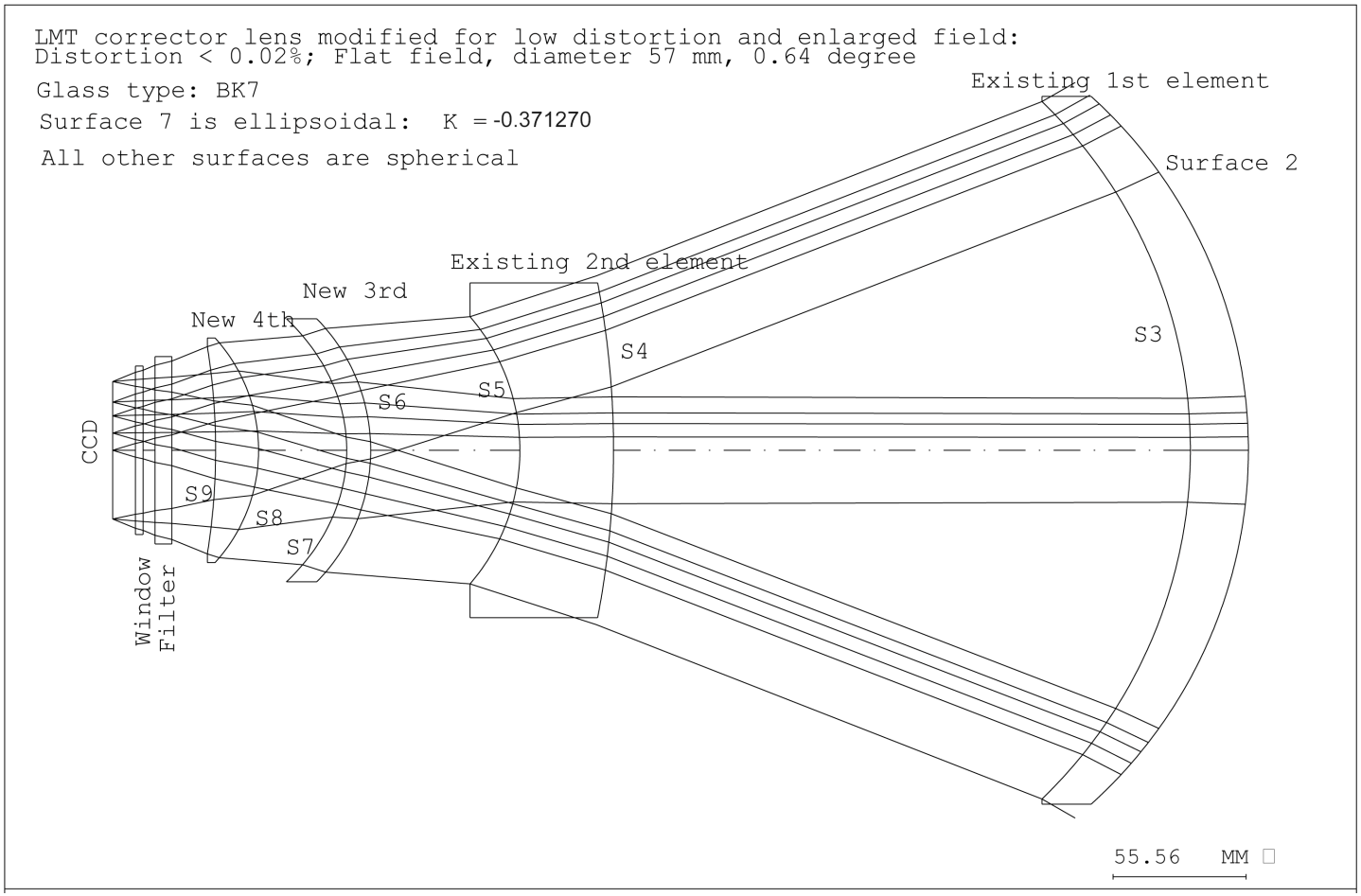

Figure IV.I.1-5. Optical layout of the modified 4-element field corrector installed on the 3.0 m f/1.5 NASA-LMT. The CCD, camera head window, and filter are also shown. The field distortion was removed and the useable field extended by replacing the original 3rd element with a doublet. Surface 7 (S7) is an aspheric ellipsoid. Courtesy E.H. Richardson.

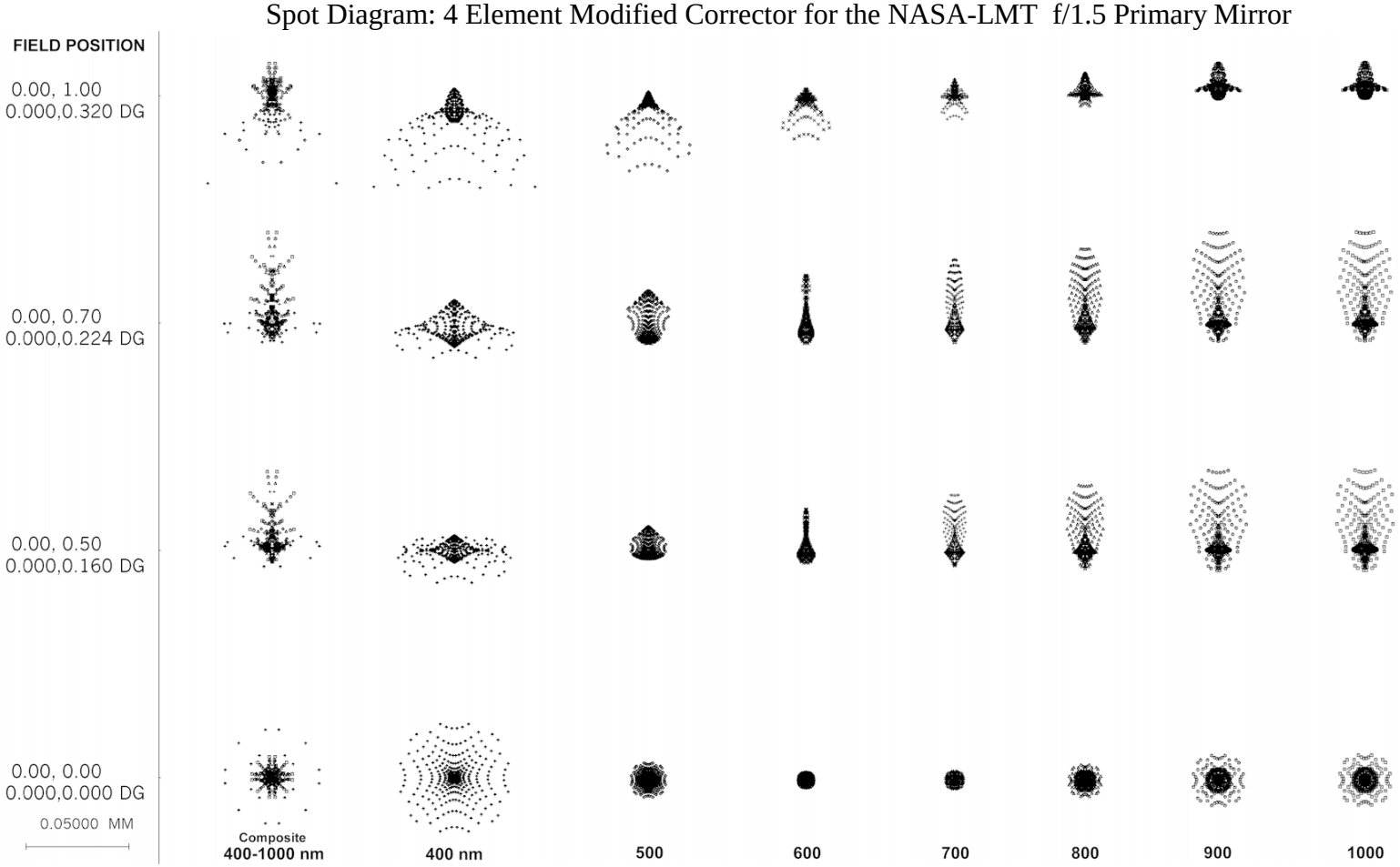

Figure IV.I.1-6. Spot diagram illustrating the optical performance of the 3.0 m f/1.5 NASA-LMT fitted with the modified 4-element corrector. The scale bar (lower left) is 50 um or 2.083 pixels on the 24um PV2K CCD, equivalent to 2.0 arcsec (effective focal ratio of f/1.7189). The 80% encircled energy diameters are less than 0.960 arcsec (1 pixel) over the entire field of view of the PV 2K CCD (<0.37 degree radius) from 400-1000 nm. This 4 element modification has corrected the distortion exhibited by the original 3 element design. Courtesy E.H. Richardson.

Spot Diagram: Infrared Performance of the NASA-LMT 4 Element Modified Corrector

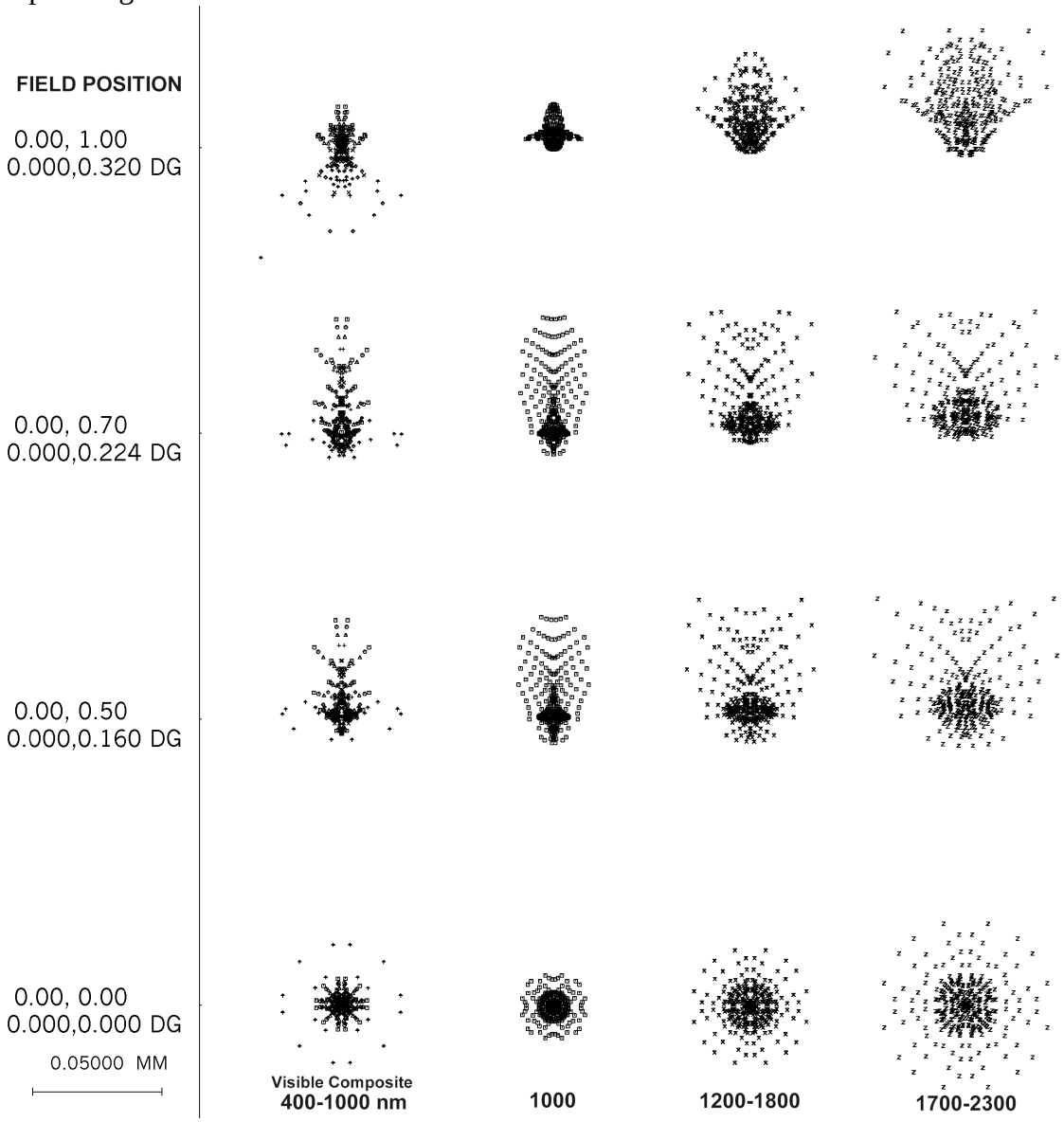

Figure IV.I.1-7. Spot diagram illustrating the excellent infrared performance of the 4 element modified NASA-LMT corrector lens. The composite visible region performance (400-1000 nm) is at left for comparison purposes. Even at 1700-2300 nm, the 80% encircled energy is less than 50 um. This is comparable to the pixel size for a near-infrared detector which may eventually be employed on the LMT. Beyond 2.3 um the transmission of the corrector's BK7 elements is negligible. Courtesy E.H. Richardson.

Optical Layout: 4 Element Corrector for the 6 m LZT f/1.5 Primary Mirror

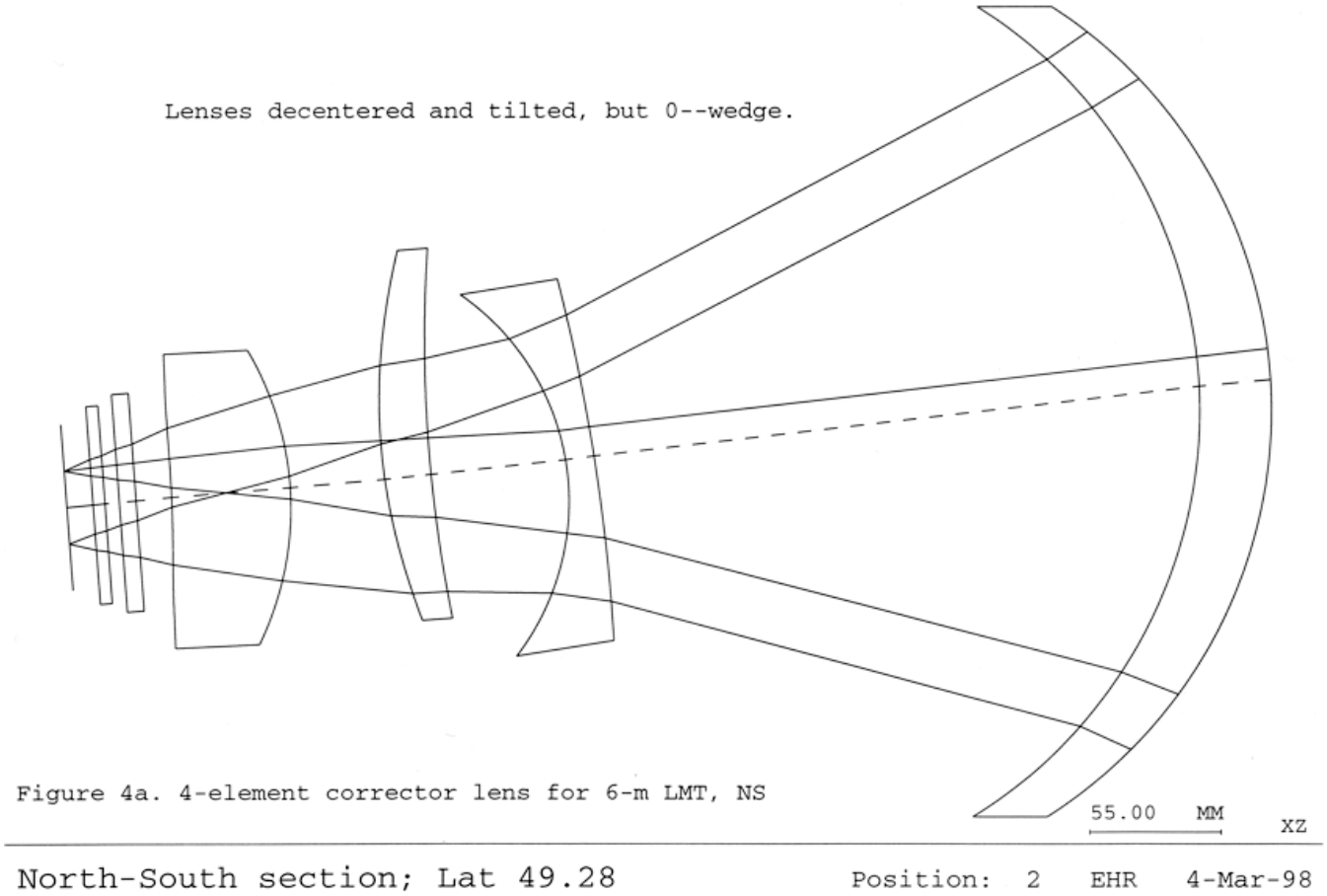

Figure IV.I.1-8. Optical layout of a 4-element field corrector proposed for the 6.0 m f/1.5 LZT. By de-centering and tilting the elements, the small-circle motion of stars can be removed to optimize the field for drift-scanning. In this example, the elements have been adjusted for the 49.28 degree latitude of the LZT test site. Courtesy Paul Hickson.

2) Detectors

Two types of detector have been employed with the NASA-LMT. CCDs were used initially for both astronomy and orbital object detection, but due to the previously discussed (Chapter II) limitations of excess selectivity and poor detection rate in DM (drift-matching) mode and the reduced sensitivity while sidereal drift-scanning, Micro-Channel Plate (MCP) Intensified video cameras were introduced in early 1996 to replace the CCDs for orbital object detection. The LSP 2K CCD was shown in Chapter I and the two most recent MCP intensified video cameras are shown in Figure IV.I.2-1. Table IV.I.2-1 lists the parameters characterizing each camera, including the new PV 2K CCD.

Sidereal scanning CCD data is acquired at a rate between 96.8 and 309 MB/hour depending on the CCD used. A Unix workstation controls the CCD via the TDITOOL SW developed by Hickson which allows real-time display of the incoming data with variable rate selection, optional sky subtraction and smoothing, resolution and astrometry output, and FITS (Flexible Image Transport System) image extraction. As will be briefly discussed in Chapter VII, TDITOOL can also detect near earth objects (NEOs) in real time. All CCD data is recorded to hard drives and then archived to Exabyte Tape.

MCP intensified video camera data is recorded to both a commercial Sony Digital Video (DV) Recorder and a High Resolution 8 mm (Hi8) Video Recorder simultaneously. These data are sent periodically to NASA-JSC for automated processing with a video data streak detector (Hebert et al.1999).

40 mm and 25 mm MCP Intensified Video Cameras

Figure IV.I.2-1. Views of two of the Micro Channel Plate (MCP) Intensified video cameras employed with the NASA-LMT for the detection of orbital objects. The upper detector utilized a 40 mm 2nd generation (G2) MCP with a 15% quantum efficiency photo-cathode and yielded a limiting magnitude of 16.5 and a 0.44 degree FOV. It was used at NODO in 1997 and 1998. The lower detector, used since 03/1999, utilizes a 25 mm 3rd generation (G3) MCP with a 33 % quantum efficiency gallium-arsenide (GaAs) photo-cathode and yields a limiting magnitude of 17.5 and a 0.275 degree FOV. The same Sony DCR-PC7 Digital Video (DV) camcorder, optically coupled to the different MCPs, is used in both cases to record the data. The 40 mm MCP in the upper camera was kindly loaned to NASA by Paul Hickson and UBC.

Table IV.I.2-1. NASA-LMT CCD and MCP-Video Detector Parameters

A	B	C	D	E	F	G	H	I	J	K	L	M
Detector	Array Size (pix)	Pixel Size (um)	Plate Scale (arcsec /pix)	FOV (arc minute)	BndWth (nm) @ >10% QE	<QE> [Peak QE]	Dyn Rnge ADU (Bit)	Full Well (e-)	Read Noise (e-)	V mag Limit	Exposure (sec) [frame/s]	Date Of Use
LSP 2K CCD (Ford Frnt Illum)	2048 x 2048	15	0.600	20.48	450-975	18 % [40]	4096 (12)	80K	28.1	~21.0	97.6 [1.4max]	5/94-7/96
PV1K CCD (SITe; Bk Illum)	1024 x 1024	24	0.960	16.38	320-1000	50 % [85]	65.5 K(16	350 K	15	~21.5	78.0 NA	3/98-7/00
PV2K CCD (SITe; Bk Illum)	2048 x 2048	24	0.960	32.77	320-1000	50 % [85]	65.5 K	300 K	11	~22.3	156.0 NA	Install 2000
ITT G2 40mm MCP Fiber Cpl'd to Video CCD	500 x 488 (circle)	65 x 50	2.6 x 2.1	21.7 x 17.1 (rect)	400-700	12 % [15]	256 (8)	NA	NA	~16.0	1/30-1/60 [30]	04/96 to 04/97
ITT G2 25 mm MCP w/DV Cam	~500 (circle)	50	2	16.66	330-600	18 [20]	256 (8)	NA	NA	~16.5	1/30-1/60 [30]	4/97-6/97
ITT G2 40mm MCP w/DV Cam	~800 (circle)	50	2	26.66	400-700	12 % [15]	256 (8)	NA	NA	~16.5	1/30-1/60 [30]	10/97-1/99
ITT G3 25mm MCP w/DV Camera	~1250 (circle)	20	0.8	16.66	480-880	33 [37]	256 (8)	NA	NA	~17.5	1/30-1/60 [30]	3/99-present

3) Prime Focus (PF) Superstructure and Positioning

The elements of the prime focus (PF) assembly must be accurately and rigidly positioned above the liquid primary mirror. This is accomplished by using lateral and vertical motion stages to orient the detector and corrector relative to each other and relative to the mirror. A rotation stage with 0.01 degree resolution is employed as well so that the CCD read-out direction can be aligned with the sidereal motion of the stars for drift-scanning or aligned with the position angle of motion of an orbital object if DM mode is selected. The entire assembly is mounted atop a circular ring positioned near the focal point which is supported by a tetrapod anchored to the four corners of the NODO pier. Figure IV.I.3-1 shows a view of the PF assembly as seen looking upward from the edge of the liquid mirror. Alternate views were shown in Chapter II.

Since the corrector and detector have a fixed spacing specified by the corrector optical design, they do not require separate adjustment (other than CCD rotation) but rather can be aligned as a unit with spacing and planarity tolerances set during manufacturer of the PF assembly. The lateral and vertical stages thus move the detector and corrector together relative to the mirror, as do the three screws which tilt the entire assembly. As described in detail in Chapter V, the axis of the PF assembly must be laterally aligned to within approximately 50um of the mirror optical axis to prevent image degradation, and tilt alignment should be within a few arcseconds. The allowable focal range under good seeing conditions is only a few microns.

Because the detector-corrector separation is small (~40 mm), thermal expansion

NASA-LMT @ NODO: Prime Focus Assembly

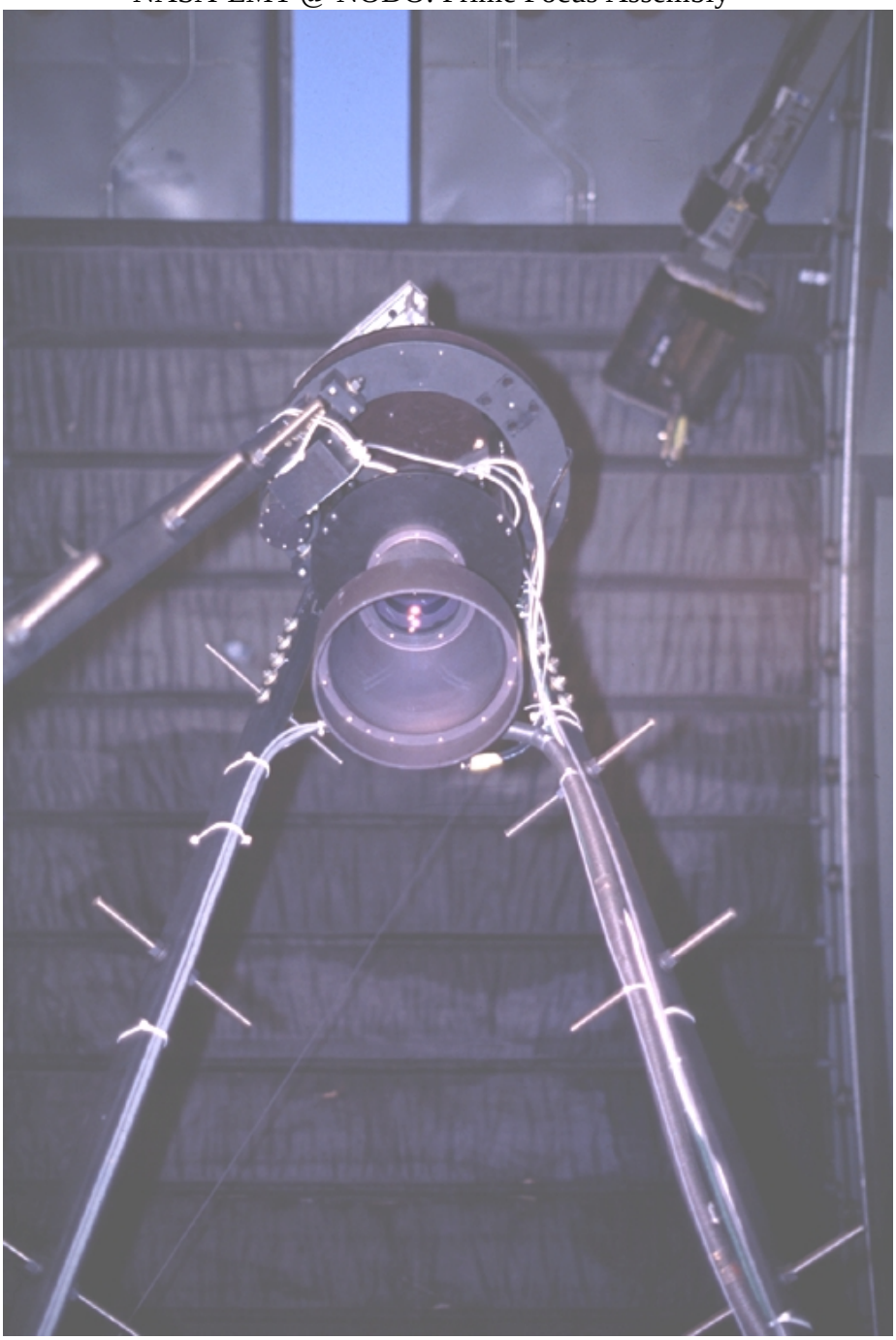

Figure IV.I.3-1. View the NASA-LMT prime focus (PF) assembly from the level of the mirror with three of the four supporting legs in place. The partially opened NODO dome slit is visible in the background as is the crane and a portion of the windscreen. The interior of the corrector lens is visible through the first element. The horizontal rungs are used for access to PF for filter and detector changes and occasional adjustments to lateral and tilt alignment which are not yet controlled remotely.

and contraction yield a negligible (~1 um/^0C) variation in spacing. This is not the case for the overall supporting structure which is comprised of HSLA (high strength low alloy) steel and extends approximately 4.8 meters above the mirror and thus has as linear vertical motion due to thermal changes of approximately 55 um/^0C . This motion is compensated by the vertical motion (focus) stage which moves the PF assembly toward or away from the mirror throughout a night's observations in accordance with temperature changes. Control of this stage and CCD rotation are directed from the control room so that correction can be applied without interrupting observations. Focus corrections can be made in 1um increments and are based on the subjective quality of images viewed with a small time delay (~30 second) if CCD drift-scanning is performed, or in real time if the MCP intensified video camera is employed. Thermistors placed on the PF support structure and throughout the observing area also give an indication of the rate and direction of temperature changes so that focus changes can be anticipated. They can also identify the existence of strong thermal gradients which can affect dome seeing.

The supporting structure can be temperature compensated by using construction materials with a small CTE such as INVAR or by regulating the structure temperature with a circulating fluid. Both options are being considered for the new PF array being built to accommodate the new PV 2K CCD. The new PF assembly will also contain a filter wheel and a linear table upon which the PV 2K CCD and MCP cameras will be mounted. The linear stage and the filter wheel will be remotely controlled thus obviating the present system whereby filter and detectors changes are made by ascending to PF.